

Evidence of *P*-wave Pairing in $\text{K}_2\text{Cr}_3\text{As}_3$ Superconductors from Phase-sensitive Measurement

Zhiyuan Zhang^{1,2,†}, Ziwei Dou^{1,†}, Anqi Wang^{1,2,†}, Cuiwei Zhang^{1,2,†}, Yu Hong^{1,2},
Xincheng Lei^{1,2}, Yue Pan^{1,2}, Zhongchen Xu^{1,2}, Zhipeng Xu^{1,2}, Yupeng Li¹, Guoan Li^{1,2},
Xiaofan Shi^{1,2}, Xingchen Guo^{1,2}, Xiao Deng^{1,2}, Zhaozheng Lyu¹, Peiling Li¹, Faming Qu^{1,2},
³, Guangtong Liu^{1,3}, Dong Su^{1,2}, Kun Jiang^{1,2,3}, Youguo Shi^{1,2,3,*}, Li Lu^{1,2,3,*}, Jie Shen^{1,3,*},
Jiangping Hu^{1,4,5,*}

¹Beijing National Laboratory for Condensed Matter Physics and Institute of Physics, Chinese
Academy of Sciences, Beijing 100190, China

²University of Chinese Academy of Sciences, Beijing 100049, China

³Songshan Lake Materials Laboratory, Dongguan, Guangdong 523808, China

⁴Kavli Institute of Theoretical Sciences, University of Chinese Academy of Sciences, Beijing,
100190, China

⁵New Cornerstone Science Laboratory, Shenzhen 518054, China

* Corresponding authors. E-mails: ygshi@iphy.ac.cn, lilu@iphy.ac.cn, shenjie@iphy.ac.cn,
jphu@iphy.ac.cn

[†]These authors contributed equally to this work.

Abstract

P-wave superconductors hold immense promise for both fundamental physics and practical applications due to their unusual pairing symmetry and potential topological superconductivity. However, the exploration of the *p*-wave superconductors has proved

to be a complex endeavor. Not only are they rare in nature but also the identification of *p*-wave superconductors has been an arduous task in history. For example, phase-sensitive measurement, an experimental technique which can provide conclusive evidence for unconventional pairing, has not been implemented successfully to identify *p*-wave superconductors. Here, we study a recently discovered family of superconductors, $A_2Cr_3As_3$ ($A = K, Rb, Cs$), which were proposed theoretically to be a candidate of *p*-wave superconductors. We fabricate superconducting quantum interference devices (SQUIDs) on exfoliated $K_2Cr_3As_3$, and perform the phase-sensitive measurement. We observe that such SQUIDs exhibit a pronounced second-order harmonic component $\sin(2\phi)$ in the current-phase relation, suggesting the admixture of 0- and π -phase. By carefully examining the magnetic field dependence of the oscillation patterns of critical current and Shapiro steps under microwave irradiation, we reveal a crossover from 0- to π -dominating phase state and conclude that the existence of the π -phase is in favor of the *p*-wave pairing symmetry in $K_2Cr_3As_3$.

Main text

The well-established BCS theory adequately explains that in low- T_c superconductor the phonon-mediated many-body electron-electron interaction leads to *s*-wave symmetry order parameter with spin-singlet pairing. However, the nature of the pairing mechanism in high- T_c superconductor remains one of the most intriguing puzzles in condensed matter physics, and promotes the development of methodology for the pairing symmetry experiments. Among these, the phase-sensitive measurements (PSMs), which provide direct evidence for the pairing phase instead of e.g., amplitudes, has settled the key controversy for the unconventional order parameter¹. One of the most established PSMs is to construct a Josephson junction (JJ) or SQUID based on the unconventional superconductor with specific

geometries and orientations. In this case, the anomaly of the unconventional pairing potential, in particular the π -phase across the lobes of the pair wave function with different signs, shifts or deforms the current-phase relation (CPR) of the JJ, and thus is featured by the unusual diffraction pattern of JJ or interference pattern of SQUID. For instance, the minima, instead of the maxima for the conventional superconductivity, of critical current I_c from JJ or SQUID crossing the corner of YBCO appears at zero-field, corresponding to the appearance of π -phase shifting between orthogonal direction. The PSM thus contributes mainly to the confirmation of the predominantly $d_{x^2-y^2}$ wave symmetry in YBCO²⁻⁴. Furthermore, other PSMs involving different crystallographic orientations, e.g. the grain boundary, reveal the coexistence of 0- and π -phases by the quasi-double-periodic CPR and I_c oscillations of the SQUIDS⁵⁻⁸. This leads to the spontaneous currents and bistable states, providing a strategy to build a so-called “quiet” qubit^{9,10}.

Different from even-parity s - or d -wave pairing, odd-parity p -wave pairing possesses spin-triplet state with spin = 1. It has attracted great attention due to the unique pairing symmetry and parity, as well as the feasibility to host Majorana zero modes in the vortex core and to construct further fault-tolerant topological quantum computation¹¹⁻¹³. Though the natural p -wave bulk superconductor is rare, there are several candidates, such as non-centrosymmetric superconductor β -Bi₂Pd¹⁴, heavy-fermion metal UTe₂¹⁵ and so on. Artificial hybrid systems have also been proposed to realize p -wave-like superconductivity, promoting extensive studies about topological materials, semiconductor nanowire with spin-orbit coupling, and ferromagnetic atom coupled to s -wave superconductor¹³. However, no solid-state p -wave system has yet been unambiguously identified because the conclusive smoking-gun experimental evidence is still lacking (The superfluid helium-3¹⁶ is beyond the system discussed here).

Recently, $A_2Cr_3As_3$ ($A = K, Rb, Cs \dots$) family is theoretically predicted to exhibit p -wave pairing¹⁷⁻²⁰. Due to the reduced dimension in the quasi-one-dimensional (Q1D) structure^{21,22} and the contribution of $3d$ orbitals of transition metal chromium atoms²³, $A_2Cr_3As_3$ family possesses strong electron-electron correlation²⁴ with a superconducting transition temperature $T_c \sim 6.1$ K at ambience pressure²¹. A series of experimental explorations have shown its unconventional superconducting signatures^{21,22,25}. The electrical transport measurement reveals a large upper critical field, both parallel and perpendicular to c -axis, exceeding the BCS weak-coupling Pauli limit^{21, 26}. NMR measurements suggest $K_2Cr_3As_3$ with spin-triplet superconductivity with the \mathbf{d} vector along c -axis²⁵. All the specific-heat data, London penetration depth revealed by a tunnel-diode-based self-inductive technique, NMR investigation and μ SR measurements support the existence of node in the superconducting gap for $K_2Cr_3As_3$ ^{22, 27-30}. Most of the experimental observations are related to the shape or amplitudes of superconducting gap, which might be modified externally by e.g., defects. Consequently, the phase-sensitive measurements, which are only related to the intrinsic phase of the pairing order parameter, are in demand.

As proposed theoretically¹¹, the ideal phase-sensitive measurement for testing the π -phase in a p -wave superconductor is to construct a superconducting loop which connects the opposite facets of the p -wave superconductor, as sketched by Supplementary Fig. 1a. In this case, there is a π -phase difference between the s - p and p - s boundaries, inducing a half magnetic flux quantum in the loop. We name it as the “polar SQUID”, which mimics the term “corner SQUID” for d -wave-YBCO phase-sensitive measurement¹. However, in realistic devices even if designed strictly as the theoretical polar SQUID, since the interfaces between s -wave (aluminum here) and p -wave candidate ($K_2Cr_3As_3$ here) are not perfectly straight (Supplementary Fig. 1c) and atomically-smooth (Supplementary Fig. 1d) proved by images of transmission electron microscope (TEM) (Supplementary Fig. 2), supercurrent flowing

through all the possible facets instead of just along the c -axis provides the admixture of 0- and π -phases (Similar situation was discussed also in d -wave YBCO PSM³¹). Therefore, we term them, as well as the derived configuration in Supplementary Fig. 1e, as the “quasi-polar SQUIDs”.

We fabricate such quasi-polar SQUID with two aluminum (Al) - $\text{K}_2\text{Cr}_3\text{As}_3$ JJs and measure the interference pattern of critical current I_c as a function of perpendicular magnetic field B at different temperature T below T_c of Al and $\text{K}_2\text{Cr}_3\text{As}_3$. The $I_c(B)$ oscillation displays a traditional pattern for the asymmetric SQUID above $T = 1$ K³², while a cusp-like suppression appears at the maxima of each oscillating period at $T < 0.9$ K, behaving like an additional modulation superimposed to the normal B -dependent periodic I_c oscillation. Both fast Fourier transform (FFT) analysis and quantitative fitting using the model of two-JJ asymmetric SQUID reveal that it is due to the significant contribution from the second-order harmonic component $\sin(2\varphi)$ in CPR, whose amplitude reaches up to above half of the first-order component $\sin(\varphi)$. Such dominant $\sin(2\varphi)$ component beyond the ballistic limit for a normal JJ is the key observation of this work. It arises from the superposition of 0- and π -phase supercurrent in the SQUID which reduces the first harmonic while enhances the second harmonic. Therefore, the observation of such dominant $\sin(2\varphi)$ state entails the presence of π -phase supercurrent caused by unconventional pairing. This 0- π phase admixture also leads to the intrinsically bistable states at $\pm\varphi$ and is commonly called φ -phase state³³⁻³⁵. The accurate value of φ depends on the ratio of first (I_1)- and second (I_2)-order harmonic components ($g = I_2/I_1$) – that is also the weight of 0- and π -phase components. Moreover, we also demonstrate the modulation of the φ -phase pattern (or g) by B , and a crossover from 0-dominating to π -dominating phase state signified by the nearly double-periodic I_c oscillation^{5,8,36}. Furthermore, AC Josephson effect under microwave irradiation manifests the remarkable half-integer Shapiro steps³⁶⁻³⁹ at zero field and extending to the entire B -dependent oscillating period, in

agreement with the appearance of the dominant $\sin(2\varphi)$ components³⁹. The above-mentioned measurements also help us to exclude any extrinsic mechanism, such as ferromagnetism, as the source of π -phase. In conclusion, the PSMs here demonstrate undoubtedly the π -phase in the pairing wave function of $\text{K}_2\text{Cr}_3\text{As}_3$. Combining with the theoretical predictions^{17-20,23} and previous experiments^{21,22,25-30}, our results further support this material as a p -wave bulk superconductor.

$\text{K}_2\text{Cr}_3\text{As}_3$ (the crystal structure is sketched in Figs. 1a and b) possesses double-walled tube along c -axis, separated by two kinds of K^+ cations with different bonding angles^{17-19,22}. Such a typical Q1D structure^{21,22} is helpful for the exfoliation of the materials and the further advanced device fabrication. As shown in Fig. 1c, the quasi-polar device (also sketched in Supplementary Fig. 2e, the reason why we use this configuration is listed in Supplementary Information Sec 4) consists of a $\text{K}_2\text{Cr}_3\text{As}_3$ stripe exfoliated from the bulk crystal and Al loop deposited afterwards (the growth and fabrication details are in Supplementary Information Secs. 1 and 2). The cross-section of $\text{K}_2\text{Cr}_3\text{As}_3$ stripe is more parallelogram- or trapezoid-like due to the lattice structure^{22,40}. It is obvious that the current of the SQUID flows through both JJ_A and JJ_B , while JJ_C is connected in series with the SQUID due to the superconducting shortcut by $\text{K}_2\text{Cr}_3\text{As}_3$ below (see more evidence in Supplementary Information Sec. 12). The zoomed-in sketch in Fig.1c highlights the detailed structure of the JJ, which contains the SiO_2 barrier at the two opposite “b-facets” reducing the current through these facets (see the details in Supplementary Figs. 2e and 3a). Fig. 1c also shows the measurement configuration with standard lock-in technique at a dilution refrigerator. The real device is shown in Fig.1d. By cooling down from 7 K to ~ 10 mK, we find there are two transitions in the differential resistance dV/dI vs T curve in Fig. 1e: the first happens at $T \sim 4$ K, indicating T_c of $\text{K}_2\text{Cr}_3\text{As}_3$ stripe, and another at 1.2 K corresponding to T_c of Al. The superconducting transition slope of $\text{K}_2\text{Cr}_3\text{As}_3$ stripe is not as sharp as that of the bulk crystal, which might be due to the slight

aging effect^{21,41}. Most of our measurement is performed at $T < 1.2$ K to make sure the supercurrent appears in JJs composed by $K_2Cr_3As_3$ and Al.

In JJs with transmission t , the CPR acquires higher harmonics and is usually sufficient to consider the first two harmonics³². The conventional supercurrent is in the “0-state”^{4,33}, because its phase-dependent supercurrent $I(\phi)$ is zero and the Josephson energy $U(\phi)$ ($U(\phi) \propto \int I(\phi)d\phi$) is minimal at $\phi = 0$ (magenta curves in Fig. 1f). Once the unconventional superconductivity is involved¹, additional π phase appears and results in a “ π -state”, which has the minimal Josephson energy at $\phi = \pi$ (blue curves in Fig. 1f)^{4,33}. In realistic devices, due to different crystal facets involved in the junctions, both 0- and π -states could possibly contribute to the total CPR. In such admixture of 0- and π -states, a “ ϕ -states” emerges, where its first harmonic can be made arbitrarily small by adjusting the weight of its 0- and π -phase components^{4,33}. In particular, the second harmonic is consequently enhanced and $g = I_2/I_1$ may significantly exceed 1/2 which is impossible for individual 0- or π -state, even reaching the perfect ballistic limit⁵⁻⁹. As a result, the CPR for the ϕ -state shows characteristic quasi- π -period oscillation and the Josephson energy $U(\phi)$ has two degenerate energy minimal points at $\phi = \pm \arccos(1/2g)$ (black curves in Fig. 1f), instead of only one in the 0- or π -states (magenta and blue curves in Fig. 1f). Such two degenerate energy minimal points also result in a spontaneously generated current in the JJ - an important signature for the unconventional superconducting pairing state, and can be harnessed to construct a quiet qubit because of the intrinsic bistable states¹⁰. The dominant second harmonic (or $g > 1/2$) is a key signature for ϕ -states^{4,33,35}, accompanied by the appearance of an intermediate maxima (or a kink) between the main maxima in CPR as shown in Fig. 1f. Such phenomena have been studied extensively in YBCO grain-boundary JJs^{1,5,6,8} and superconductor-ferromagnet-superconductor (S-F-S) JJs³⁶, as well as considered as a common result of the coexistence of 0- or π -states^{33,36}.

This dominant second harmonic, or the φ -states, can be directly investigated using a SQUID. As illustrated in Fig. 1c, the SQUID contains two junctions A and B in parallel, each with the CPR in the generic form of $I_1 \sin(\varphi) - I_2 \sin(2\varphi)$. The phases across each junction are determined by the magnetic flux threading the loop and the phase drops across the inductance in each arm. Therefore, the total CPR for the SQUID can be modeled as follows^{5,8,36}:

$$I_{tot}(\varphi_A, \varphi_B) = [I_{A1} \sin(\varphi_A) - I_{A2} \sin(2\varphi_A)] + [I_{B1} \sin(\varphi_B) - I_{B2} \sin(2\varphi_B)] \quad (1A)$$

$$\varphi_A - \varphi_B + 2\pi L[I_A(\varphi_A) - I_B(\varphi_B)]/\Phi_0 = 2\pi\Phi/\Phi_0 \quad (1B)$$

For a fixed flux Φ , the critical current $I_c(\Phi) = \max [I_{tot}(\varphi_A, \Phi)]$ calculated by equation (1) can be compared directly with the experimental results to extract the harmonics I_{A1} , I_{A2} , I_{B1} , I_{B2} . The extraction of the harmonics can be made easier if one junction has much higher critical current than the other, and shape of $I_c(\Phi)$ is simply the CPR of the weak junction³². Therefore, equation (1A) can be simplified as:

$$I_{tot}(\varphi_A, \varphi_B) = [I_{A1} \sin(\varphi_A) - I_{A2} \sin(2\varphi_A)] + I_{B1} \sin(\varphi_B) \quad (2)$$

In Supplementary Information Sec. 3, we demonstrate that for the SQUID the presence of both 0- and π -state in the p -wave section between two junctions, which is what the quasi-polar SQUID here is designed to detect, also suppresses the first harmonic while enhances the second harmonic, exactly equal to that in the junctions.

Fig. 1g (black curve) illustrates the expected SQUID oscillation when the system is in the φ -state. Different from the 0- or π -state SQUID oscillations (magenta and blue curves in Fig. 1g, respectively), the maximal I_c is not exactly at $\Phi = 0$ or $\Phi_0/2$ and the location depends on g . Moreover, within one period of oscillation $I_c(\Phi)$ two peaks instead of one are clearly visible, which is the key signature of the presence of φ -state. We note that a large screening factor $\beta = LI_c/\Phi_0 = 0.45$, while shifting the curve in the flux and making the shape of $I_c(\Phi)$ more skewed, does not alter the qualitative features mentioned before (black dashed-curve in Fig.1g). We also note that for SQUIDs with high transmission JJs but without φ -state (that is, close but not

beyond the ballistic limit, $g \leq 1/2$) cannot produce the double-peak oscillations since it includes all even and odd higher harmonics⁴², while the φ -state enhances the even harmonics and suppresses the odd harmonics. As shown in Supplementary Secs. 4 and 5, due to the involvement of different facets, both 0- and π -state supercurrents exist in a quasi-polar SQUID and result in the φ -state. Therefore, the π -state (necessarily included in φ -state) can be experimentally detected by the enhanced second harmonics and the characteristic double-peak oscillations in $I_c(\Phi)$ in the quasi-polar SQUIDs.

To directly test whether such φ -state (or more precisely π -state) exists in our device, we measured the I_c vs B oscillation of the SQUID at different T (Fig. 2). The interference pattern at high T ($T = 1, 1.1$ K in Figs. 2d, e) exhibit a slightly tilted and shifted oscillation with respect of B and current bias I_{DC} due to the inductance of the SQUID (see Supplementary Information Sec. 9). The measured period of the I_c oscillation is around 0.058 mT, which translates to an effective SQUID area of $34.5 \mu\text{m}^2$, close to the designed geometry around $32 \mu\text{m}^2$ (see Supplementary Information Sec. 2). Gradually, a dip appears at the maxima and the oscillation splits into quasi-double-periodic when $T < 0.9$ K. Such quasi-double-periodic oscillation is reproducible for different cooldown processes with close-to-zero magnetic field to exclude the effect of random vortex pinning (see Cooldown 1 and 2 in Fig. 2). To get the quantitative result, we calculate the Fourier expansion of the I_c oscillation and plot the coefficients $F_{1,2}$ vs T in Fig. 2f. These results give a general description of the amplitudes of the first- and second-harmonic terms, respectively⁶. Apparently, F_2 increases drastically with decreasing T and reaches above half of F_1 around $T = 0.8$ K (see F_1/F_2 in Fig. 2h), which is consistent with the appearance of quasi-double-periodic feature in the $I_c(B)$ curves in Fig. 2e.

Moreover, we fit the experimental data with the two-JJ asymmetric SQUID model as discussed in equation (2) (see the typical fitting results as shown by the yellow curves in Figs. 2a-d and Supplementary Fig. 9). The resulted T -dependent coefficients for the two JJs

respectively are listed in Fig. 2g, with an additional value of I_c for JJ_B (the strong junction) compared to the Fourier coefficients. (The detailed fitting results for each T and discussion are in Supplementary Information Sec. 9, with $L = 88$ pH and another two parameters $\Delta\phi_2$ and $\Delta\phi_S$ probably arising from the spontaneous current, which have been discussed in YBCO and S-F-S ϕ -junction^{11,33,34,43-47}.) Except that, the first and second-harmonic terms $I_{A1, A2}$ have the similar value and T -dependence to $F_{1,2}$, showing that these two quantitative analysis methods are reasonable and accurate. Based on these, there are two conclusions here: 1. $g > 1/2$ when $T < 0.9$ K (Fig. 2h), revealing the coexistence of 0 and π -phase components in the SQUID at low T ; 2. For JJ_A (the weak junction), I_{A1} decreases and I_{A2} increases, which means the π -phase component becomes larger with decreasing T . Such strong T -dependent behavior is commonly observed in YBCO-based JJ and is possibly related to the local properties of the devices⁸, such as the distribution of current along different facets⁴⁷, the transparency-dependent coupling to different wavefunction^{1,31}, and the varying stress of two materials in the junctions⁴⁸. Meanwhile, we emphasize that we find similar behavior for different cooldown processes from the same device (see Cooldown 1 and 2 in Fig. 2). We also reproduce such ϕ -state SQUIDs in seven devices (Supplementary Information Sec. 10 and Supplementary Figs. 11 and 12). All these prove the robustness of 0- and π -phases in the quasi-polar SQUID, which is consistent with the fact that the predicted p -wave pairing results in 0- or π -phase along the different directions, for example, parallel to ab -plane or c -axis as pointed out by the magenta/blue arrows in Fig. 1c^{17-20,23}.

More interestingly in the ϕ -state SQUID, the weight of 0- and π -phase components is able to vary the sign of the first-harmonic term through a sweet spot with equal 0 and π -phase components, where there is no first term and a double-periodic (π - instead of 2π -periodic) CPR. By applying stronger B , we find the oscillation pattern changes drastically as other YBCO junctions show^{5,8} and one-peak reappears at high magnetic field as illustrated in Fig.

3a (also see the zoomed-in oscillation at different B in Fig. 3b). The aforementioned double-periodic structure shows up around $B \sim 0.5$ mT (the arrow in Fig. 3a, upper plot), which is similar to a I_c dip (the arrow in Fig. 3a, lower plot) possibly rising from the φ -state Fraunhofer pattern^{8,34,49}. Such dip in the Fraunhofer pattern slightly different from zero field has also been observed in d -wave YBCO junctions with both 0- and π -phase supercurrent flowing in different facets^{8,34,49}. We also notice the pattern is point symmetric with respect of $B = 0$ regardless of the detailed 0- and π -phase mixture (see more data at different T in Supplementary Fig. 7)^{8,34,49}. Similarly, we use both the FFT and SQUID model analysis for each period at different B (Figs. 3b, c and Supplementary Fig. 10), and show the detailed results in Figs. 3d-f. Indeed, the two kinds of results match each other, and F_1 , I_{A1} , F_2/F_1 and I_{A2}/I_{A1} all have a kink at $B \sim 0.5$ mT, consistent with the sign change of the first term at the sweet spot (The gradual evolution of the first and second terms from FFT is clearly illustrated in Fig. 3c). That is, below/above $B = 0.5$ mT, the 0-phase component is bigger/smaller than π -phase component, and the first term has positive/negative sign. All these behaviors show that the sweet spot represents a dominant 0- to π -phase transition. More measurements about B -dependent pattern with different sweeping directions are listed in Supplementary Information Sec. 11, with the intention to ruling out ferromagnetism as the source of the observed π -phase in Al-K₂Cr₃As₃ SQUIDs.

Such a quasi-double-periodic I_c oscillation could also arise from the beating of the two single-periodic oscillations with different periods⁵⁰, apart from the enhanced second harmonics ($g > 1/2$) due to the admixture of 0- to π -phases. To further confirm whether the enhanced second harmonics indeed exists, we measure the I - V curves under microwave irradiation, where half-integer Shapiro steps should appear in this case. Here, the phase-locked response to the irradiation at a given frequency produces a series of quantized steps in voltage (or Shapiro steps) as a result of the AC Josephson effect. Therefore, for the JJ with the

CPR such as $I_1 \sin(\varphi) - I_2 \sin(2\varphi)$, the first harmonic produces the integer Shapiro steps $V_n = nhf/2e$ ($n = \pm 1, \pm 2, \pm 3, \dots$), while the second harmonic produces the half-integer Shapiro steps $V_n = nhf/4e$ ($n = \pm 1, \pm 2, \pm 3, \dots$)³⁹, which are what we intend to observe. In the past, such method has been applied to investigate the half-integer harmonic contents in systems such as φ -junction state in d -wave JJs^{5,8,37}, ferromagnetic JJs^{36,38} and in the newly discovered twisted BSCCO JJs⁴³, high transmission SNS junction using high-mobility graphene or semiconductor^{42,51,52} (here $g \leq 1/2$) and enhanced higher harmonics due to non-equilibrium process⁵³. We note that in our overdamped junctions (see Supplementary Figs. 19 and 20) the association between half-integer Shapiro steps and second harmonic of CPR is straightforward without complications due to the chaotic phase-lock dynamics³⁹.

In the experiment, it is more common to measure the Shapiro map, tracing the dependence of the differential resistance dV/dI as a function of the a.c. and d.c. current drive (I_{AC} and I_{DC} respectively). Fig. 4a shows a typical theoretical Shapiro map calculated by the widely used RSJ model detailed in Supplementary Information Sec. 13. The conventional integer current steps are clearly visible. Furthermore, for $|g| = |I_2/I_1| = 1.2$ same as the values at $T = 0.1$ K extracted in Fig. 2h, the $1/2$ step emerges between the two sequential integer steps, corresponding to the dominant second harmonic in φ -state. In Fig. 4b, we measure such Shapiro map at $B = 0$, $T = 0.1$ K and $f = 4.69$ GHz (or $\nu = f/f_J \approx 0.35$, $I_c = 4.6$ μ A, $R_N = 6.0$ Ω , $f_J = 2eI_c R_N/h$ being the Josephson frequency³⁹). The Shapiro map shows the qualitatively similar features as the theoretical map in Fig. 4a, in particular a clear $1/2$ step (red arrow). The high I_{DC} region of the map is somewhat distorted by an addition JJ (JJ_C) outside the SQUID which we carefully distinguish in Supplementary Fig. 18, but does not affect the qualitative feature at low I_{DC} region. By integrating the measured $dV/dI(I_{DC})$ and obtaining the histogram of the I - V curves for each P in Fig. 4c, the steps are better illustrated and the clear peak at $V = (1/2)nhf/2e$ (magenta arrow) is seen. The typical I - V curve showing clear $1/2$ step is shown in

Supplementary Fig. 21d. As shown in Fig. 4d taken at different T , such $1/2$ step at zero magnetic field persists up to at least 0.5 K and becomes blurred above 0.7 K, which is similar to the temperature range where g decreases from above to below $1/2$ with higher T in Fig. 2h and thus proves they are cogenetic.

By fixing the microwave power and sweeping the magnetic field, we can further observe the evolution of the half-integer step as a function of the flux. Fig. 4e is the $dV/dI(I_{DC}, B)$ data taken without microwave irradiation at $T = 0.1$ K, showing clearly the double-peak feature. By introducing the microwave with $f = 4.69$ GHz ($P = 16$ dBm, corresponding to the magenta vertical dashed line in Fig. 4b), the $1/2$ step is continuous throughout the whole period of the SQUID (Figs. 4f, g). In addition to the data shown here, in Supplementary Fig. 21c, we reproduce such $1/2$ step in another similar device (Device B) using the similar $\nu = \nu = f/f_J \approx 0.35$ which is also continuous throughout the whole SQUID period.

We note several scenarios where the $1/2$ step may appear without φ -state ($g < 1/2$), which we exclude as follows. First, a high frequency comparable to f_J or a high power above the first node will induce half Shapiro step even when $g < 1/2$, as both f and P will enhance the width of the $1/2$ step³⁹. However, in Fig.4 and Supplementary Fig. 21, we show that for the low microwave frequency $\nu = f/f_J = 0.35$ used here the half-integer steps at low power before the first node occurs, and thus can be used as an indicator for $g > 1/2$ in our system. Second, the half-inter steps here disappear at higher temperature, accompanied by the degradation of double-peak oscillation, which is inconsistent with second-harmonic caused by the microwave-induced non-equilibrium where they still survive at higher T ⁵³. Finally, the half-integer Shapiro step at low frequency and power may also arise in SQUIDs without φ -state. However, it occurs only around the flux $\Phi \approx \Phi_0/2$ where the first harmonic of the two JJs is much reduced due to destructive interference, and thus g becomes larger than $1/2$ ⁵⁴⁻⁵⁶. On the contrary, the $1/2$ step in Fig.4 and Supplementary Fig. 21 is continuous throughout the whole

period, in particular at zero flux, thus excluding such interference mechanism. In conclusion, these confirm beyond doubt that the $1/2$ Shapiro steps observed here indeed originate from a dominant second harmonic ($g > 1/2$), or the φ -state, in the SQUID. In particular, the comparison between positive and negative bias in Device B clearly shows that double-peak feature and the half-integer Shapiro steps in the whole period appear/disappear simultaneously with the negative/positive bias (Supplementary Fig. 21c), demonstrating the close correlation between them. This further eliminates the interpretation of the quasi-double-periodic $I_c(B)$ as the beating between two single-periodic oscillating channels⁵⁰, since the beating effect does not induce large second harmonics. Therefore, the measured quasi-double-periodic $I_c(B)$, as well as the robust half-integer Shapiro steps, can only be caused by the co-existence of 0- and π -phases supercurrent.

Meanwhile, the unconventional π -phase component may originate from several mechanisms beside p -wave superconductivity, such as ferromagnetism³⁶ and multi-band coupling between s -wave components^{22, 29, 57}. First, previously experiments observed the non-static spin-fluctuations with the short-range spin configurations flipping on the atomic scale. However, this does not produce a static long-range ferromagnetic order and thus the π -phase supercurrent in our micron-sized device either. Second, as more data shown in Supplementary Information Sec. 11, no hysteresis or mirror-symmetry in $I_c(B)$ is observed between up and down sweeps of B , thus demonstrating the absence of any ferromagnetism in the system. Besides ferromagnetic states, exotic s -wave states, such as a variety of sign changed s -wave states proposed for iron-based superconductors⁵⁸, cannot be applicable to the π -phase supercurrent observed in our device because the sign change is in the momentum space and it does not produce the sign change in real space. Exotic pairings between different bands in $\text{K}_2\text{Cr}_3\text{As}_3$ is extremely difficult to form since the dispersions and Fermi surfaces of these three bands in $\text{K}_2\text{Cr}_3\text{As}_3$ are very different^{17, 19}. Therefore, we are left with the unconventional p -

wave superconductivity as the cause for the π -phase component. As for the type of p -wave pairing, we have discussed in Supplementary Information Sec. 5. In these quasi-polar devices, the phase of the supercurrent is less sensitive to p -wave pairing along the a/b -axis than the c -axis and thus the π -phase supercurrent might be mainly from c -axis, which is supported in particular by the strongly B -modulated 0 and π -components in Fig. 3. More data show the comparison between a quasi-polar SQUID along the c -axis, a quasi-polar SQUID along the a/b axis, and an edge SQUID fabricated on the same $\text{K}_2\text{Cr}_3\text{As}_3$ crystal. Around zero field, the quasi-double-periodic $I_c(B)$ only appears in the quasi-polar SQUID along the c -axis, which also indicate the π -phase from c -axis is more predominant than that from the a/b -axis (Supplementary Information Sec. 5). However, we still need more evidence to prove the type of p -wave pairing, which is beyond the scope of this manuscript. We reproduce the quasi-double-periodic $I_c(B)$ in seven quasi-polar SQUID devices (Devices A-G, Supplementary Figs. 11 and 12), while five more devices do not show such feature (F1-5, Supplementary Information Sec. 10). While the devices are fabricated by similar procedures, the degradation with the dissipation of K element (shown by EDS in Supplementary Fig. 14), the different crystal dimensions, the anisotropic etching, and the unintentional deposition of SiO_2 sputtered from the substrate by the etching ions⁵⁹ (Supplementary Fig. 2) result in a different quality of the Al- $\text{K}_2\text{Cr}_3\text{As}_3$ interfaces, which affects s - p coupling⁶⁰ and the weight of the π -phase component.

In conclusion, we have measured quasi-double-periodic $I_c(B)$ oscillation at low temperature and attribute this to the enhanced second-order harmonic component $\sin(2\varphi)$. This anomalous $\sin(2\varphi)$ has also been proved by the significant half-integer Shapiro steps appearing in the entire B -dependent period and reveals the coexistence of 0- and π -phases. Apart from temperature, magnetic field also modules the weight of 0- and π -phase components, and induces a dominant 0- to π -phase transition. By varying the sweeping

direction of the magnetic field, we can exclude any ferromagnetic component as the source of the π -phase here. The appearance of π -phase, which is reproducible in multiple devices, demonstrates the sign change in the superconducting pairing order parameter, and is consistent with predicted p -wave pairing in $\text{K}_2\text{Cr}_3\text{As}_3$. Such a φ -phase SQUID pattern is possibly more convincing than that of pure π -phase SQUID. The reason is that it superimposes a pattern on the original 0-phase SQUID oscillation, instead of shifting the entire pattern by half of B period, which might arise from the residual magnetic field in the magnet, the vortex pinning in the device or the inductance of the loop. This Q1D p -wave superconductor with the advantages of desirable superconducting transition temperature at ambient pressure and compatibility of the state-of-the-art lithography technique provides an ideal platform to develop novel superconducting devices and qubits.

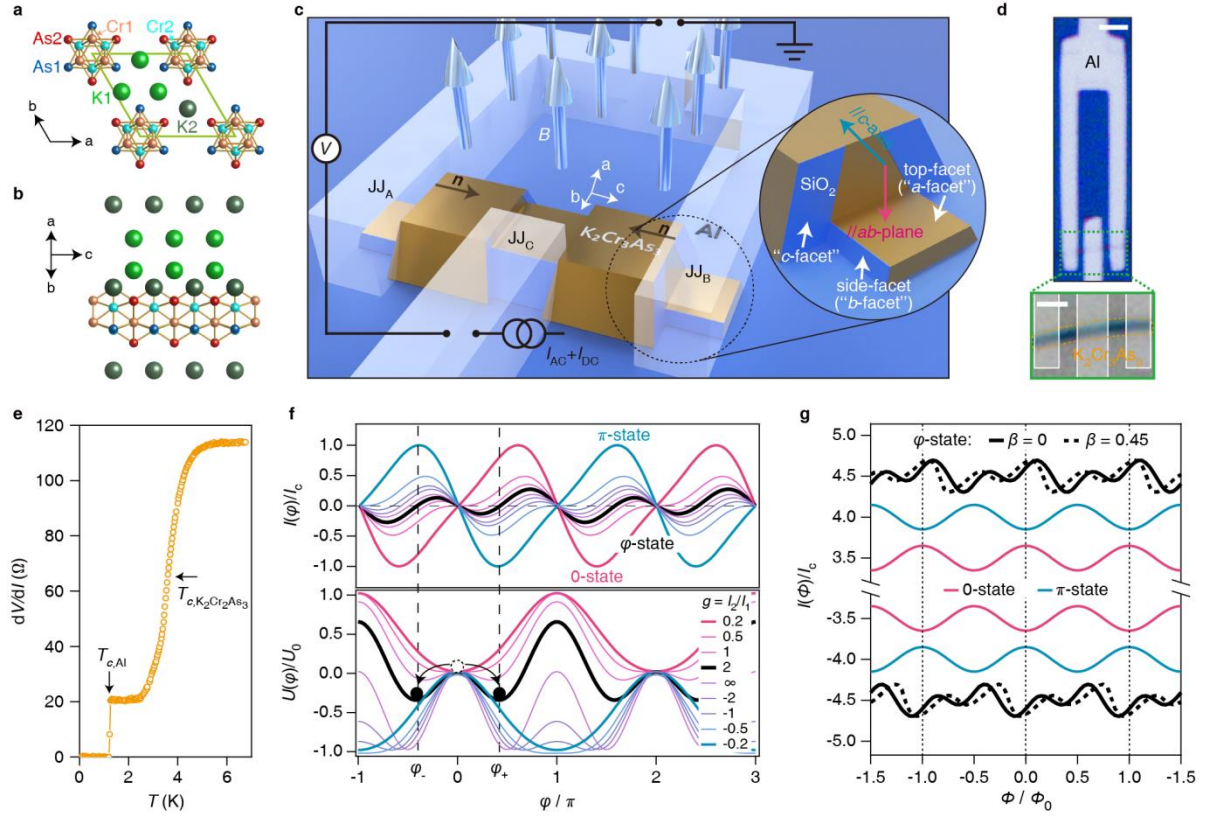


Fig. 1 Phase-sensitive measurement of $K_2Cr_3As_3$ SQUID. **a, b,** Crystal structure of $K_2Cr_3As_3$: **a**, top view perpendicular to the c -axis. **b**, side view parallel to the c -axis. **c**, Cartoon of the $K_2Cr_3As_3$ SQUID with Al contacts and measurement configuration. Inset: zoomed-in JJ with a thin layer of sputtered dust of SiO_2 onto the etched surfaces. The three etched surfaces pointed out by the white arrows are defined as “a/b/c-facets”, respectively. The supercurrent flowing via the ab -plane and c -axis are marked in magenta and blue, respectively, in JJ_A and JJ_B combining into the SQUID, with JJ_C connected in series. **d**, Optical image of the real device (scale bar: 2 μm) with the zoomed-in junction area (green rectangle, scale bar: 1 μm). **e**, $R = dV/dI$ versus T showing a slow superconducting transition around 4 K for $K_2Cr_3As_3$ and a sharp transition at 1.2 K for Al. **f**, CPR (upper) and Josephson energy (lower) for various $g = I_2/I_1$. When $|g| < 0.5$, the system only has one stable state at either $\varphi = 0$ (0-state, $g < 0$) or $\varphi = \pi$ (π -state, $g > 0$). When $|g| > 0.5$, the system has two stable states at $\varphi_{\pm} = \pm \arccos(1/2g)$ (φ -state²⁹), which also corresponds to a dominant second

harmonic in the CPR. **g**, The critical current of the SQUID I_c versus the flux Φ . Magenta: 0-state, blue: π -state, black: generic φ -state which is a mixture of 0 and π -state. The “double-peak” structure only appears in φ -state SQUID. Dashed line: φ -state SQUID with inductance effect increasing the misalignment between I_{c+} and I_{c-} . $\beta = LI/\Phi_0 = 0.45$.

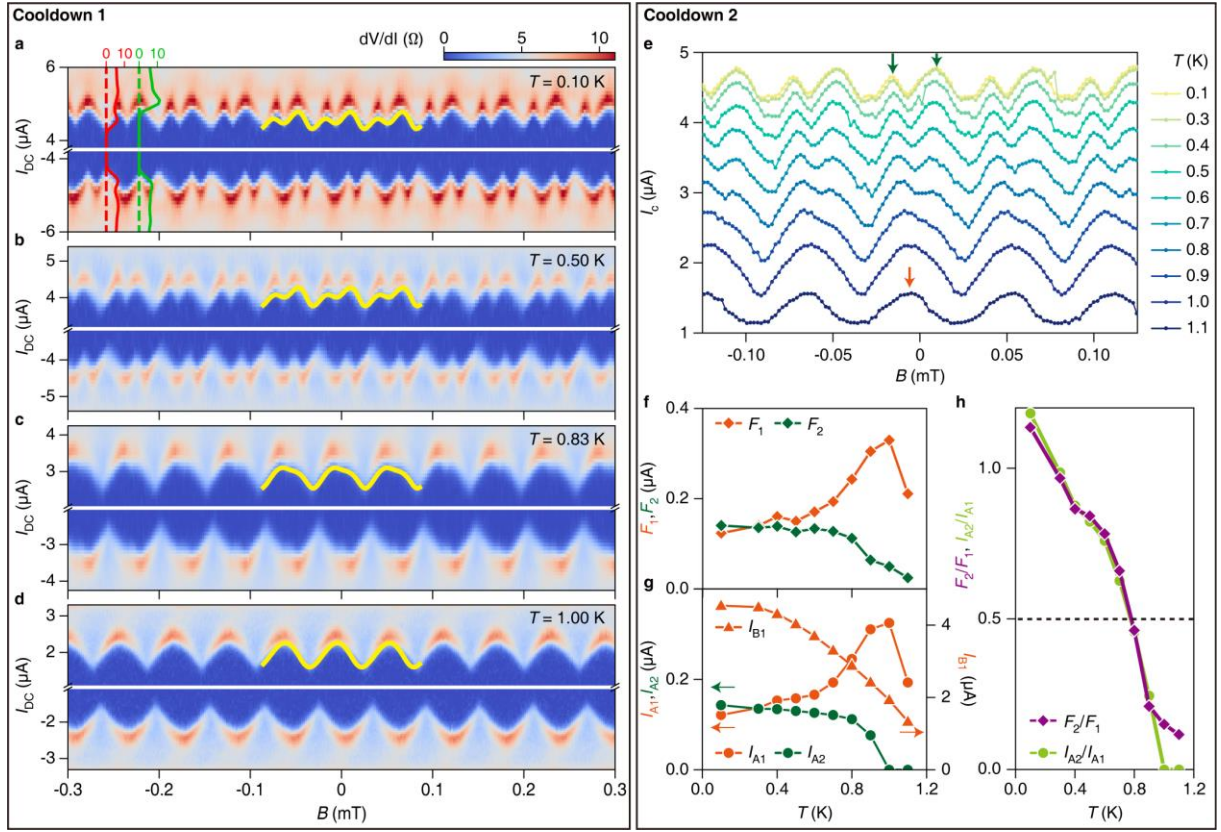


Fig. 2. Flux-dependent critical current at different temperatures. **a-d**, $R = dV/dI$ versus I_{DC} and B at $T = 0.10, 0.50, 0.83$ and 1.00 K, respectively (more data in Supplementary Fig. 6). For each temperature, I_{DC} sweeps in the positive/negative direction. The typical $dV/dI - I_{DC}$ linecuts at the minimal (red curve) and maximal (green curve) I_c are marked in **a**. The dark-blue regime in the 2D map has zero-resistance, with the I_c signed by red. The quasi- “double-periodic” I_c structure in each period is obvious at for $T \leq 0.83$ K, reflecting the dominating second harmonic component (see text). At $T = 1.0$ K, this is reduced to the single peak shape (dominated by the first harmonic). The fitting results of $I_c(B)$ are overlapped for all the figures. **e**, $I_c(B)$ extracted from $dV/dI(I_{DC}, B)$ with better temperature resolution between 0.1 and 1.1 K in another cooldown. The transition from the single-periodic (orange arrow) to the quasi-double-periodic (green arrows) oscillations is reproduced. **f**, The first and the second FFT components (F_1, F_2) of $I_c(B)$ versus T for the second cooldown. Details is in Supplementary Information Section 8. **g**, I_{A1}, I_{A2} for JJ_A and I_{B1} for JJ_B versus T from the

fitting (see text). Details is in Supplementary Information Section 9. **h**, F_1/F_2 (purple) and $g = I_{A2}/I_{A1}$ (prasinous) versus T . g exceeds 1/2 below 0.8 K.

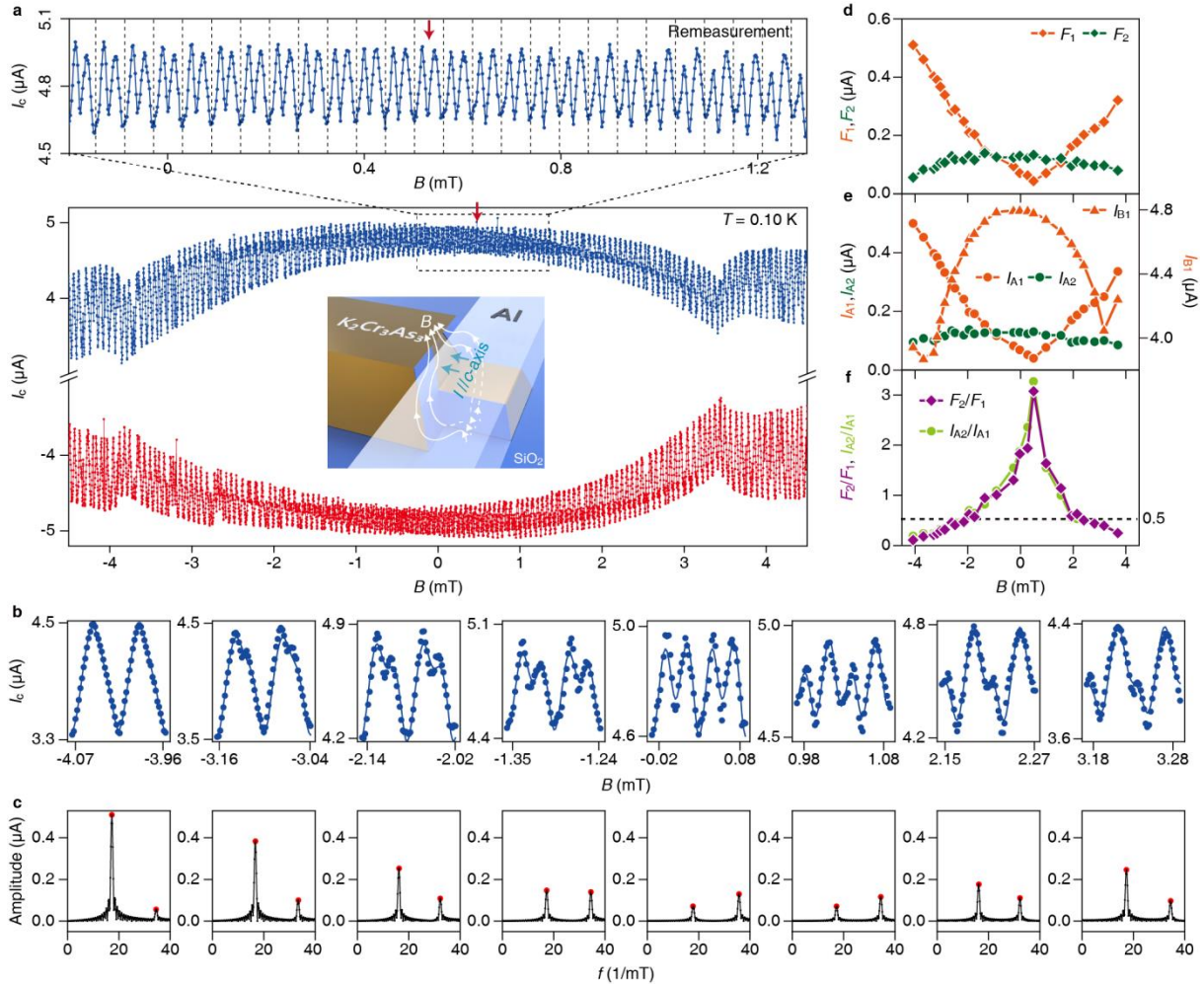


Fig. 3 Flux-dependent critical current at wide range of magnetic field. **a**, Positive and negative critical current $I_{c\pm}(B)$ at $T = 0.1$ K, showing double-to-single periodic transition. Upper plot: the remeasured zoomed-in plot across the transition region for B from -0.2 mT to 1.3 mT. Red arrows: B with the largest ratio between the second and first harmonics (upper plot) and the dip in the Fraunhofer pattern (lower plot). More data is in Supplementary Fig. 7. Inset: The illustration of distorted magnetic field lines wrapping around $K_2Cr_3As_3$ at the interface between the Al film and $K_2Cr_3As_3$. **b**, measured $I_c(\Phi)$ at different B (blue dots) with the fitting curves of the SQUID model (blue lines). **c**, Corresponding FFT amplitude spectrum of $I_c(\Phi)$, showing the first two harmonics. The first and the second FFT components F_1 and F_2

are extracted at the red points. **d**, The first and the second FFT components (F_1 , F_2) versus B . **e**, $I_{A1,2}$ and I_{B1} from the fitting versus B . **f**, F_1/F_2 (purple) and $g = I_{A2}/I_{A1}$ (prasinous) versus T . g exceeds 1/2 for $|B|$ within 2 mT.

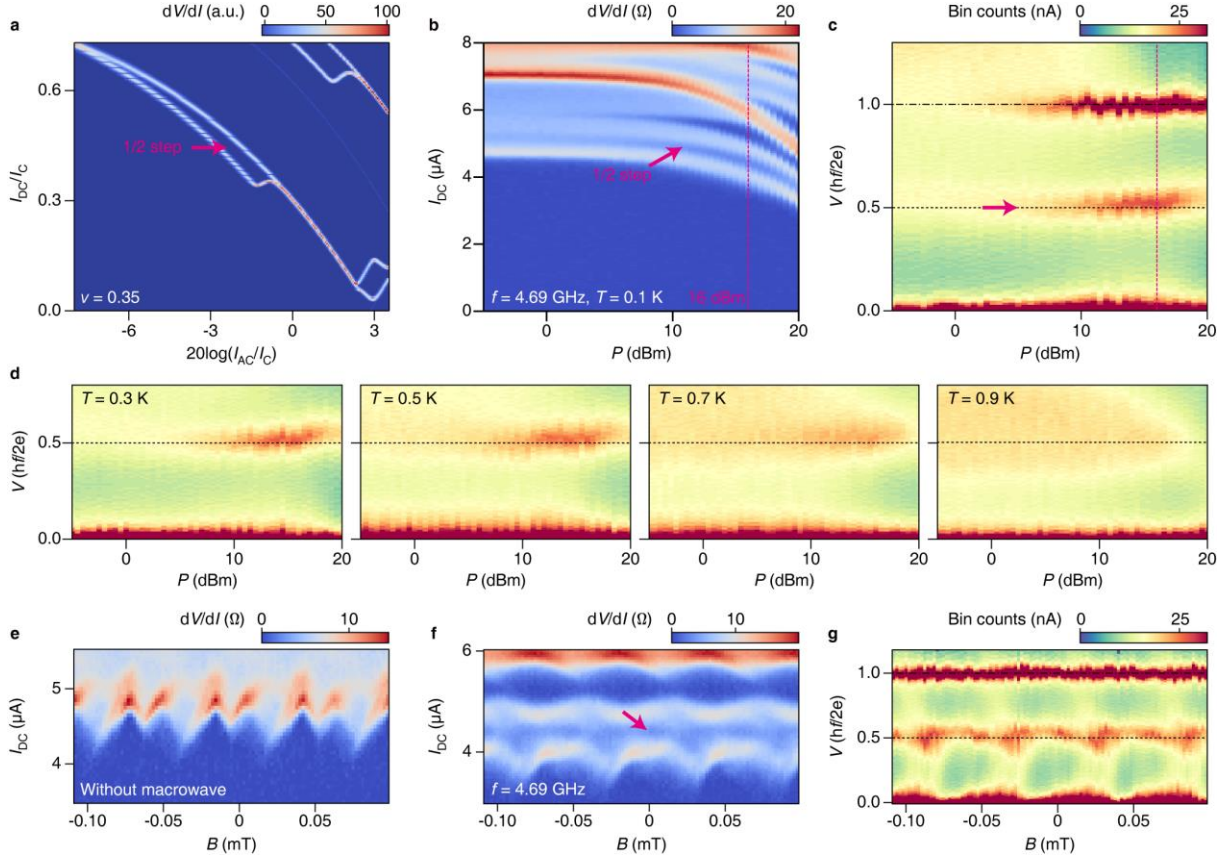


Fig. 4. Dominant second harmonic demonstrated with fractional Shapiro step. **a**, The calculated Shapiro maps showing half-integer steps between subsequent integer steps for $g = |I_2/I_1| = 1.2$ similar to Fig. 2h at $T = 0.1$ K for $\nu = 0.35$. The $1/2$ step (magenta arrow) appears between integer steps. **b**, $R = dV/dI$ versus I_{DC} and microwave power P . The microwave frequency $f = 4.69$ GHz ($\nu = f/f_J \approx 0.35$), $B = 0$ T, $T = 0.1$ K. The $1/2$ step is seen, in agreement with **a**. The evolution of the $1/2$ step with power is measured only up to 20 dBm due to the maximal power provided by the microwave source. **c**, Histogram obtained from the integrated I - V curve versus V and P further showing the clear $1/2$ step at zero field. **d**, Histograms versus V and P at $B = 0$ T from $T = 0.3$ to 0.9 K. $f = 4.69$ GHz. The $1/2$ step is clear below 0.5 K and diminishes at higher temperatures. **e**, $dV/dI(I_{DC}, B)$ at $T = 0.1$ K without irradiation. **f**, $dV/dI(I_{DC}, B)$ with $f = 4.69$ GHz and $P = 16$ dBm (vertical magenta dashed line in **b**). The $1/2$ step (the magenta arrow) is continuous throughout the whole period. **g**, histogram also showing the continuous $1/2$ step.

Data availability

All data needed to evaluate the conclusions in the paper are present in the main text and/or the supplementary information. Raw data generated in this study are available from the corresponding author upon reasonable request.

Acknowledgement

The work of J.S., L.L., F.Q. and G.L. was supported by the Beijing Natural Science Foundation (Grant No. JQ23022), the Strategic Priority Research Program B of Chinese Academy of Sciences (Grant No. XDB33000000), the Beijing Nova Program (Grant No. Z211100002121144), the National Natural Science Foundation of China (Grant Nos. 92065203 and 12174430), and the Synergetic Extreme Condition User Facility (SECUF). The work of K. J. and J. H. was supported by the Ministry of Science and Technology (Grant No. 2022YFA1403900), the National Natural Science Foundation of China (Grant No. NSFC-11888101, No. NSFC-12174428, No. NSFC-11920101005), the Strategic Priority Research Program of the Chinese Academy of Sciences (Grant No. XDB28000000, XDB33000000), the New Cornerstone Investigator Program, and the Chinese Academy of Sciences Project for Young Scientists in Basic Research (2022YSBR-048). The work of Y.S. was supported by the National Natural Science Foundation of China (Grants No. U2032204), the Informatization Plan of Chinese Academy of Sciences (CAS-WX2021SF-0102), and the Strategic Priority Research Program of the Chinese Academy of Sciences (Grants No. XDB33030000).

Author contributions

J.P.H. and J. S. conceived and designed the experiment.

Z.Y.Z., Z.W.D., A.Q.W., Y.H., Y.P.L., G.A.L., X.F.S., X.C.G., and X.D. fabricated devices and performed the transport measurements, and discussed with Z.Z.L., P.L.L., F.M.Q., G.T.L, supervised by L.L., J.S. and J.P.H..

C.W.Z., Z.C.X., and Y.G.S. grew $\text{K}_2\text{Cr}_3\text{As}_3$ single crystals.

X.C.L., Y.P., and D.S. performed the STEM measurements.

Z.Y.Z., Z.W.D., and Z.P.X. performed the theoretical analysis, supervised by K.J., J.S., and J.P.H..

Z.Y.Z., Z.W.D., A.Q.W., J.S., and J.P.H. analyzed the data and wrote the manuscript, with input from all authors.

Competing interests

Authors declare that they have no competing interests.

References

1. Van Harlingen, D.J.: Phase-sensitive tests of the symmetry of the pairing state in the high-temperature superconductors - evidence for $d_{x^2-y^2}$ symmetry. Rev. Mod. Phys. 67, 515–535 (1995).
2. Wollman, D.A., Van Harlingen, D.J., Lee, W.C., Ginsberg, D.M., Leggett, A.J.: Experimental determination of the superconducting pairing state in YBCO from the phase coherence of YBCO-Pb dc SQUIDs. Phys. Rev. Lett. 71, 2134–2137 (1993).
3. Wollman, D.A., Van Harlingen, D.J., Giapintzakis, J., Ginsberg, D.M.: Evidence for $d_{x^2-y^2}$ pairing from the magnetic field modulation of YBa₂Cu₃O₇-Pb Josephson junctions. Phys. Rev. Lett. 74, 797–800 (1995).
4. Tsuei, C.C., Kirtley, J.R.: Pairing symmetry in cuprate superconductors. Rev. Mod. Phys. 72, 969–1016 (2000).
5. Lindström, T., Charlebois, S.A., Tzalenchuk, A.Y., Ivanov, Z., Amin, M.H.S., Zagorskin, A.M.: Dynamical effects of an unconventional current-phase relation in YBCO dc SQUIDs. Phys. Rev. Lett. 90, 117002 (2003).
6. Il'ichev, E., Grajcar, M., Hlubina, R., IJsselsteijn, R.P.J., Hoenig, H.E., Meyer, H.-G., Golubov, A., Amin, M.H.S., Zagorskin, A.M., Omelyanchouk, A.N., Kupriyanov, M.Y.: Degenerate ground state in a mesoscopic YBa₂Cu₃O_{7-x} grain boundary Josephson junction. Phys. Rev. Lett. 86, 5369–5372 (2001).
7. Brawner, D.A., Ott, H.R.: Evidence for an unconventional superconducting order parameter in YBa₂Cu₃O_{6.9}. Phys. Rev. B, 50, 6530–6533 (1994).
8. Lindström, T., Johansson, J., Bauch, T., Stepanov, E., Lombardi, F., Charlebois, S.A.: Josephson dynamics of bicrystal d -wave YBa₂Cu₃O_{7-δ} dc-SQUIDs. Phys. Rev. B 74, 014503 (2006).
9. Bauch, T., Lindström, T., Tafuri, F., Rotoli, G., Delsing, P., Claeson, T., Lombardi,

- F.: Quantum dynamics of a d -Wave Josephson junction. *Science* 311(5757), 57–60 (2006).
10. Amin, M.H.S., Smirnov, A.Y., Zagoskin, A.M., Lindström, T., Charlebois, S.A., Claeson, T., Tzalenchuk, A.Y.: Silent phase qubit based on d -wave Josephson junctions. *Phys. Rev. B* 71, 064516 (2005).
 11. Geshkenbein, V.B., Larkin, A.I., Barone, A.: Vortices with half magnetic flux quanta in “heavy-fermion” superconductors. *Phys. Rev. B* 36, 235–238 (1987).
 12. Ivanov, D.A.: Non-Abelian statistics of half-quantum vortices in p -wave superconductors. *Phys. Rev. Lett.* 86, 268–271 (2001).
 13. Flensberg, K., Oppen, F., Stern, A.: Engineered platforms for topological superconductivity and Majorana zero modes. *Nat. Rev. Mater.* 6(10), 944–958 (2021).
 14. Li, Y., Xu, X., Lee, M.-H., Chu, M.-W., Chien, C.L.: Observation of half-quantum flux in the unconventional superconductor β -Bi₂Pd. *Science* 366(6462), 238–241 (2019).
 15. Jiao, L., Howard, S., Ran, S., Wang, Z., Rodriguez, J.O., Sigrist, M., Wang, Z., Butch, N.P., Madhavan, V.: Chiral superconductivity in heavy-fermion metal UTe₂. *Nature* 579(7800), 523–527 (2020).
 16. Lee, D. M.: The extraordinary phases of liquid ³He. *Rev. Mod. Phys.* 69, 645 (1997).
 17. Wu, X., Yang, F., Le, C., Fan, H., Hu, J.: Triplet p_z -wave pairing in quasi-one-dimensional A₂Cr₃As₃ superconductors (A = K, Rb, Cs). *Phys. Rev. B* 92, 104511 (2015).
 18. Hu, J.: Novel quasi-one-dimensional chromium-based unconventional superconductors. *Science Bulletin* 60(24), 2140–2141 (2015).
 19. Zhou, Y., Cao, C., Zhang, F.-C.: Theory for superconductivity in alkali chromium arsenides A₂Cr₃As₃ (A=K, Rb, Cs). *Science Bulletin* 62(3), 208–211 (2017).
 20. Wu, X.-X., Le, C.-C., Yuan, J., Fan, H., Hu, J.-P.: Magnetism in quasi-one-dimensional A₂Cr₃As₃ (A = K, Rb) superconductors. *Chinese Physics Letters* 32(5), 057401 (2015).

21. Bao, J.-K., Liu, J.-Y., Ma, C.-W., Meng, Z.-H., Tang, Z.-T., Sun, Y.-L., Zhai, H.-F., Jiang, H., Bai, H., Feng, C.-M., Xu, Z.-A., Cao, G.-H.: Superconductivity in quasi-one-dimensional $\text{K}_2\text{Cr}_3\text{As}_3$ with significant electron correlations. *Phys. Rev. X* 5, 011013 (2015).
22. Pang, G.M., Smidman, M., Jiang, W.B., Bao, J.K., Weng, Z.F., Wang, Y.F., Jiao, L., Zhang, J.L., Cao, G.H., Yuan, H.Q.: Evidence for nodal superconductivity in quasi-one-dimensional $\text{K}_2\text{Cr}_3\text{As}_3$. *Phys. Rev. B* 91, 220502 (2015).
23. Hu, J., Cao, G., Cao, C.: Electronic structure of quasi-one-dimensional superconductor $\text{K}_2\text{Cr}_3\text{As}_3$ from first-principles calculations. *Scientific Reports* 5(1), 16054 (2015).
24. Chen, R.Y., Wang, N.L.: Progress in Cr- and Mn-based superconductors: a key issues review. *Reports on Progress in Physics* 82(1), 012503 (2018).
25. Yang, J., Luo, J., Yi, C., Shi, Y., Zhou, Y., Zheng, G.-Q.: Spin-triplet superconductivity in $\text{K}_2\text{Cr}_3\text{As}_3$. *Science Advances* 7(52), 4432 (2021).
26. Zuo, H., Bao, J.-K., Liu, Y., Wang, J., Jin, Z., Xia, Z., Li, L., Xu, Z., Kang, J., Zhu, Z., Cao, G.-H.: Temperature and angular dependence of the upper critical field in $\text{K}_2\text{Cr}_3\text{As}_3$. *Phys. Rev. B* 95, 014502 (2017).
27. Tang, Z.-T., Bao, J.-K., Liu, Y., Sun, Y.-L., Ablimit, A., Zhai, H.-F., Jiang, H., Feng, C.-M., Xu, Z.-A., Cao G.-H.: Unconventional superconductivity in quasi-one-dimensional $\text{Rb}_2\text{Cr}_3\text{As}_3$. *Phys. Rev. B* 91, 020506(R) (2015).
28. Luo, J., Yang, J. Zhou, R. Mu, Q. G. Liu, T. Ren, Z.-A., Yi, C. J., Shi, Y. G. Zheng, G.-Q.: Tuning the distance to a possible ferromagnetic quantum critical point in $\text{A}_2\text{Cr}_3\text{As}_3$ *Phys. Rev. Lett.* 123, 047001 (2019).
29. Adroja, D. T., Bhattacharyya, A., Telling, M., Feng, Y., Smidman, M., Pan, B., Zhao, J., Hillier, A. D., Pratt, F. L., Strydom, A. M.: Superconducting ground state of quasi-one-dimensional $\text{K}_2\text{Cr}_3\text{As}_3$ investigated using μSR measurements. *Phys. Rev. B* 92, 134505

(2015).

30. Zhi, H.Z., Imai, T., Ning, F.L., Bao, J.-K., Cao, G.-H.: NMR investigation of the quasi-one-dimensional superconductor $K_2Cr_3As_3$. *Phys. Rev. Lett.* 114, 147004 (2015).
31. Ariando, D., D., Smilde, H.-J.H., Leca, V., Blank, D.H.A., Rogalla, H., Hilgenkamp, H.: Phase-sensitive order parameter symmetry test experiments utilizing $Nd_{2-x}Ce_xCuO_{4-y}/Nb$ zigzag junctions. *Phys. Rev. Lett.* 94, 167001 (2005).
32. Likharev, K.K.: Superconducting weak links. *Rev. Mod. Phys.* 51, 101–159 (1979).
33. Goldobin, E., Koelle, D., Kleiner, R., Mints, R.G.: Josephson junction with a magnetic-field tunable ground state. *Phys. Rev. Lett.* 107, 227001 (2011).
34. Sickinger, H., Lipman, A., Weides, M., Mints, R.G., Kohlstedt, H., Koelle, D., Kleiner, R., Goldobin, E.: Experimental evidence of a φ Josephson junction. *Phys. Rev. Lett.* 109, 107002 (2012).
35. Goldobin, E., Koelle, D., Kleiner, R., Buzdin, A.: Josephson junctions with second harmonic in the current-phase relation: Properties of φ junctions. *Phys. Rev. B* 76, 224523 (2007).
36. Stoutimore, M.J.A., Rossolenko, A.N., Bolginov, V.V., Oboznov, V.A., Rusanov, A.Y., Baranov, D.S., Pugach, N., Frolov, S.M., Ryazanov, V.V., Van Harlingen, D.J.: Second-harmonic current-phase relation in Josephson junctions with ferromagnetic barriers. *Phys. Rev. Lett.* 121, 177702 (2018).
37. Terpstra, D., IJsselsteijn, R.P.J., Rogalla, H.: Subharmonic Shapiro steps in high- T_c Josephson junctions. *Applied Physics Letters* 66(17), 2286–2288 (1995).
38. Sellier, H., Baraduc, C., Lefloch, F.m.c., Calemczuk, R.: Half-integer shapiro steps at the 0π crossover of a ferromagnetic josephson junction. *Phys. Rev. Lett.* 92, 257005 (2004).
39. Raes, B., Tubsrinuan, N., Sreedhar, R., Guala, D.S., Panghotra, R., Dausy, H., Souza Silva, C.C., Vondel, J.: Fractional Shapiro steps in resistively shunted Josephson junctions

- as a fingerprint of a skewed current-phase relationship. Phys. Rev. B 102, 054507 (2020).
40. Mu, Q.-G., Ruan, B.-B., Pan, B.-J., Liu, T., Yu, J., Zhao, K., Chen, G.-F., Ren, Z.-A.: Ion-exchange synthesis and superconductivity at 8.6 K of $\text{Na}_2\text{Cr}_3\text{As}_3$ with quasi-one-dimensional crystal structure. Phys. Rev. Mater. 2, 034803 (2018).
 41. Xiang, J.-J., Yu, Y.-L., Wu, S.-Q., Li, B.-Z., Shao, Y.-T., Tang, Z.-T., Bao, J.-K., Cao, G.-H.: Superconductivity induced by aging and annealing in $\text{K}_{1-\delta}\text{Cr}_3\text{As}_3\text{H}_x$. Phys. Rev. Mater. 3, 114802 (2019).
 42. P. Zhang, A. Zarassi, L. Jarjat, V. Van de Sande, M. Pendharkar, J. S. Lee, C. P. Dempsey, A. P. McFadden, S. D. Harrington, J. T. Dong, H. Wu, A.-H. Chen, M. Hocevar, C. J. Palmstrøm, S. M. Frolov: Large second-order Josephson effect in planar superconductor-semiconductor junctions. SciPost Phys. 16, 030 (2024).
 43. Zhao, S.Y.F., Cui, X., Volkov, P.A., Yoo, H., Lee, S., Gardener, J.A., Akey, A.J., Engelke, R., Ronen, Y., Zhong, R., Gu, G., Plugge, S., Tummuru, T., Kim, M., Franz, M., Pixley, J.H., Poccia, N., Kim, P.: Time-reversal symmetry breaking superconductivity between twisted cuprate superconductors. Science 382, 6677 pp. 1422-1427 (2023).
 44. Mannhart, J., Hilgenkamp, H., Mayer, B., Gerber, C., Kirtley, J.R., Moler, K.A., Sigrist, M.: Generation of magnetic flux by single grain boundaries of $\text{YBa}_2\text{Cu}_3\text{O}_{7-x}$. Phys. Rev. Lett. 77, 2782–2785 (1996).
 45. Mints, R.G.: Self-generated flux in josephson junctions with alternating critical current density. Phys. Rev. B 57, 3221–3224 (1998).
 46. Tsuei, C.C., Kirtley, J.R., Chi, C.C., Yu-Jahnes, L.S., Gupta, A., Shaw, T., Sun, J.Z., Ketchen, M.B.: Pairing symmetry and flux quantization in a tricrystal superconducting ring of $\text{YBa}_2\text{Cu}_3\text{O}_{7-\delta}$. Phys. Rev. Lett. 73, 593–596 (1994).
 47. Lombardi, F., Tafuri, F., Ricci, F., Granozio, F.M., Barone, A., Testa, G., Sarnelli, E., Kirtley, J.R., Tsuei, C.C.: Intrinsic *d*-wave effects in $\text{YBa}_2\text{Cu}_3\text{O}_{7-\delta}$ grain boundary

- Josephson junctions. *Phys. Rev. Lett.* 89, 207001 (2002).
48. Wu, Y., Ying, L., Li, G.; Zhang, X., Peng, W., Ren, J., Wang, Z.: Film Stress Influence on Nb/Al-AlO_x/Nb Josephson Junctions. *IEEE Transactions on Applied Superconductivity*, 29, 5, 1102105, (2019).
 49. Bauch, T., Johansson, J., Cedergren, K., Lindström, T., Lombardi, F.: YBCO SQUIDs with unconventional current phase relation Author links open overlay panel. *Physica C* 463–465 (2007).
 50. Murani, A., Kasumov, A., Sengupta, S., Kasumov, Yu A., Volkov, V. T. Khodos, I. I. Brisset, F. Delagrangé, R., Chepelianskii, A., Deblock, R., Bouchiat, H., Guéron, S.: Ballistic edge states in Bismuth nanowires revealed by SQUID interferometry. *Nat. Commun.* 8, 15941 (2017).
 51. Huang, Z., Elfeky, B.H., Taniguchi, T., Watanabe, K., Shabani, J., Shahrjerdi, D.: Observation of half-integer Shapiro steps in graphene Josephson junctions. *Applied Physics Letters* 122(26), 262601 (2023).
 52. Ueda, K., Matsuo, S., Kamata, H., Sato, Y., Takeshige, Y., Li, K., Samuelson, L., Xu, H., Tarucha, S.: Evidence of half-integer Shapiro steps originated from nonsinusoidal current phase relation in a short ballistic InAs nanowire Josephson junction. *Phys. Rev. Res.* 2, 033435 (2020).
 53. Iorio, A., Crippa, A., Turini, B., Salimian, S., Carrega, M., Chirolli, L., Zannier, V., Sorba, L., Strambini, E., Giazotto, F., Heun, S.: Half-integer Shapiro steps in highly transmissive InSb nanoflag Josephson junctions. *Phys. Rev. Res.* 5, 033015 (2023).
 54. Li, Y., Yan, D., Hong, Y., Sheng, H., Wang, A.-Q., Dou, Z., Guo, X., Shi, X., Su, Z., Lyu, Z., Qian, T., Liu, G., Qu, F., Jiang, K., Wang, Z., Shi, Y., Xu, Z.-A., Hu, J., Lu, L., Shen, J.: Interfering Josephson diode effect and magnetochiral anisotropy in Ta₂Pd₃Te₅ asymmetric edge interferometer. *arXiv:2306.08478* (2023).

55. Mori, M., Maekawa, S.: Half-integer Shapiro-steps in superconducting qubit with a π -Josephson junction. *Applied Physics Express* 14(10), 103001 (2021).
56. Souto, R.S., Leijnse, M., Schrade, C.: Josephson diode effect in supercurrent interferometers. *Phys. Rev. Lett.* 129, 267702 (2022).
57. Wang, Z., Yi, W., Wu, Q., Sidorov, V. A., Bao, J., Tang, Z., Guo, J., Zhou, Y., Zhang, S., Li, H., Shi, Y., Wu, X., Zhang, L., Yang, K., Li, A., Cao, G., Hu, J., Sun, L., Zhao, Z.: Correlation between superconductivity and bond angle of CrAs chain in non-centrosymmetric compounds $A_2Cr_3As_3$ ($A = K, Rb$) *Scientific Reports*, 6, 37878 (2016).
58. Hu, J.: Iron-based superconductors as odd-parity superconductors. *Phys. Rev. X* 3, 031004 (2013).
59. Desbiolles, B. X. E., Bertsch, A., Renaud P.: Ion beam etching redeposition for 3D multimaterial nanostructure manufacturing. *Microsystems & Nanoengineering* 5, 11 (2019).
60. Barash, Yu. S., Burkhardt, H., Rainer, D.: Low-temperature anomaly in the Josephson critical current of junctions in d -wave superconductors. *Phys. Rev. Lett.* 77, 4070 (1996).

Supplemental Information: Evidence of *P*-wave Pairing in $\text{K}_2\text{Cr}_3\text{As}_3$

Superconductors from Phase-sensitive Measurement

Zhiyuan Zhang^{1,2,†}, Ziwei Dou^{1,†}, Anqi Wang^{1,2,†}, Cuiwei Zhang^{1,2,†}, Yu Hong^{1,2}, Xincheng Lei^{1,2}, Yue Pan^{1,2}, Zhongchen Xu^{1,2}, Zhipeng Xu^{1,2}, Yupeng Li¹, Guoan Li^{1,2}, Xiaofan Shi^{1,2}, Xingchen Guo^{1,2}, Xiao Deng^{1,2}, Zhaozheng Lyu¹, Peiling Li¹, Faming Qu^{1,2,3}, Guangtong Liu^{1,3}, Dong Su^{1,2}, Kun Jiang^{1,2,3}, Youguo Shi^{1,2,3,*}, Li Lu^{1,2,3,*}, Jie Shen^{1,3,*}, Jiangping Hu^{1,4,5,*}

¹Beijing National Laboratory for Condensed Matter Physics and Institute of Physics, Chinese Academy of Sciences, Beijing 100190, China

²University of Chinese Academy of Sciences, Beijing 100049, China

³Songshan Lake Materials Laboratory, Dongguan, Guangdong 523808, China

⁴Kavli Institute of Theoretical Sciences, University of Chinese Academy of Sciences, Beijing, 100190, China

⁵New Cornerstone Science Laboratory, Shenzhen 518054, China

* Corresponding authors. E-mails: ygshi@iphy.ac.cn, lilu@iphy.ac.cn, shenjie@iphy.ac.cn, jphu@iphy.ac.cn

[†]These authors contributed equally to this work.

Table of content

1 Single crystal growth and crystal structure of $K_2Cr_3As_3$	3
2 Device fabrication	4
3 ϕ -state SQUID as superposition between 0- and π -state SQUID.....	4
4 Quasi-polar SQUIDs for p -wave superconductivity	6
5 Possible π -phase supercurrent in c-axis.....	10
6 Fast counter measurement of $I_c(B)$ in Figure 3.....	14
7 Extended data for Figs. 2-3	15
8 Fourier analysis of $I_c(B)$	17
9 Fitting of $I_c(B)$	18
10 More devices with and without quasi-double-periodic features	22
11 Ruling out residual ferromagnetism in Al- $K_2Cr_3As_3$ SQUIDs.....	30
12 Contribution of various segments to the SQUID transport.....	35
13 Half-integer Shapiro steps in ϕ -junction	38

1 Single crystal growth and crystal structure of $\text{K}_2\text{Cr}_3\text{As}_3$

Single crystals of $\text{K}_2\text{Cr}_3\text{As}_3$ were grown with a self-flux of KAs method. First, KAs was prepared by a solid-state reaction. The stoichiometric potassium (solid, 99.95%) and arsenic (lump, 99.99%) were mixed in an Ar-filled glove box. The mixtures were loaded in an alumina crucible and then sealed in an evacuated quartz tube. The sample-loaded quartz tube was heated to 473 K for 10 hours and dwelt for 20 hours. Second, the precursor KAs powders, chromium (powder, 99.99%) and arsenic (lump, 99.99%) were mixed in a molar ratio of 6:1:1, and the mixtures were loaded in an alumina crucible. The alumina crucible (covered with a cap) was jacketed in a Ta tube, and the welded Ta tube was finally sealed in an evacuated quartz tube. The quartz tube was heated up to 1273 K and held for 24 hours in a furnace, followed by cooling down to 923 K at a rate of 2 K/h. Finally, extra flux was removed to obtain single crystals by centrifugation at 923 K. Shiny needle-like crystals were harvested. The synthesized crystals were very reactive in air and easily deteriorate at ambient conditions. These samples were kept in an argon-filled glove box¹.

$\text{K}_2\text{Cr}_3\text{As}_3$ crystallizes in a hexagonal lattice with $a = 9.9832(9) \text{ \AA}$, $c = 4.2304(4) \text{ \AA}$, and the space group of $\text{K}_2\text{Cr}_3\text{As}_3$ is $\text{P}\bar{6}\text{m}2$ (No. 187) at room temperature²⁻⁵. The prominent structural unit is the quasi-1D $[(\text{Cr}_3\text{As}_3)^{2-}]_{\infty}$ chains along the c-axis, which are arranged triangularly in the ab-plane¹⁻⁶. The chains are well separated by K^+ ions. Hence, the inter-chains coupling is expected to be much weaker than the intra-chains coupling, exhibiting a strongly 1D structure character¹⁻⁶.

2 Device fabrication

The $K_2Cr_3As_3$ is sensitive to oxygen and water¹, and thus all the microfabrication processes involving exposed crystals were done in a nitrogen-filled glove box. The K_2Cr_3As stripes were first mechanically exfoliated onto the p -doped Si substrates with SiO_2 layer and spin-coated with PMMA. The samples were transferred and covered by electron-beam deposition of AlO_x films without exposure to air. The SQUID geometries were then patterned using electron-beam lithography, with the subsequent development process also done in the glove box. Afterwards, the K_2Cr_3As stripes were etched by the argon plasma and then deposited by Al leads. After lifting off in the nitrogen-filled glove box, a layer of AlO_x was coated to protect the samples. Now with the protection layer, the samples were taken outside the glove box for wire bonding and measurement. The area of the SQUID is estimated considering the finite penetration length and field distortion effects.

3 ϕ -state SQUID as superposition between 0- and π -state SQUID

The ϕ -state can be understood as the co-existence of both 0- and π -states of the supercurrent circulating in the whole SQUID. For the conventional 0-state SQUID the total phase in the loop is simply $\varphi_A - \varphi_B + 2\pi L(I_A - I_B)/\Phi_0 = 2\pi \Phi/\Phi_0$, and the supercurrent of the SQUID is simply $I_0(\varphi_A, \varphi_B) = I_A(\varphi_A) + I_B(\varphi_B)$. Here the subscripts A and B denote the two branches of the SQUID. On the other hand, when an additional π -phase is introduced^{7,8} in the loop, a π -state SQUID is formed with $\varphi_A - \varphi_B + 2\pi L(I_A - I_B)/\Phi_0 + \pi = 2\pi \Phi/\Phi_0$ and $I_\pi(\varphi_A, \varphi_B) = I_A(\varphi_A) + I_B(\varphi_B)$. In JJs with high transmission t , the CPR acquires higher harmonics and is usually sufficient to consider the first two harmonics, then both junction A and B have two harmonics: $I_A(\varphi_A) = I_{A1} \sin(\varphi_A) - I_{A2} \sin(2\varphi_A)$ and $I_B(\varphi_B) = I_{B1} \sin(\varphi_B) - I_{B2} \sin(2\varphi_B)$.

When both 0-state and π -state supercurrent co-exist in the SQUID, the supercurrent can be written in the similar manner as the single junction (assuming B as the reference junction with

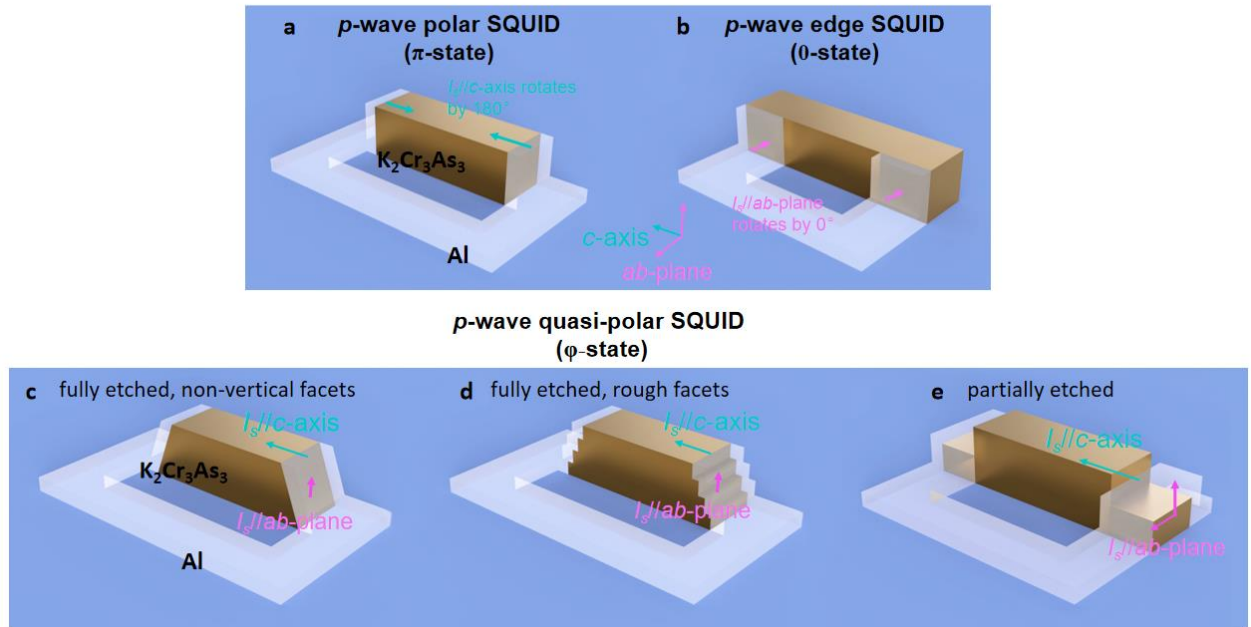
relatively higher critical current, p and q are the proportions of 0-state and π -state components, respectively):

$$\begin{aligned}
I_{tot}(\varphi_A, \varphi_B) &= pI_0(\varphi_A, \varphi_B) + qI_\pi(\varphi_A, \varphi_B) \\
&= p[I_{A1}\sin(\varphi_B - 2\pi L(I_A - I_B)/\Phi_0) - I_{A2}\sin 2(\varphi_B - 2\pi L(I_A - I_B)/\Phi_0)] \\
&\quad + q[I_{A1}\sin(\varphi_B - 2\pi L(I_A - I_B)/\Phi_0 - \pi) - I_{A2}\sin 2(\varphi_B - 2\pi L(I_A - I_B)/\Phi_0 - \pi)] + I_B(\varphi_B) \\
&= (p - q)I_{A1}\sin(\varphi_B - 2\pi L(I_A - I_B)/\Phi_0) - I_{A2}\sin 2(\varphi_B - 2\pi L(I_A - I_B)/\Phi_0) + I_B(\varphi_B) \\
&= (p - q)I_{A1}\sin(\varphi_A) - I_{A2}\sin 2(\varphi_A) + I_B(\varphi_B) \\
&= I_{A1}^* \sin(\varphi_A) - I_{A2} \sin(2\varphi_A) + I_B(\varphi_B) \quad (S1)
\end{aligned}$$

where p and q are real and positive numbers with $p+q = 1$ and $I_{A1}^* = (p - q)I_{A1}$. When the weights between the 0- and π -state are similar, the first harmonic of the junction A is much reduced as $p-q$ is much smaller than 1 while the second harmonic is not, thus producing the φ -state with $g > 1/2$.

4 Quasi-polar SQUIDs for p -wave superconductivity

Supplementary Figs. 1a, b illustrate the ideal phase-sensitive measurement for detecting p -wave superconductivity similar to the theoretical proposal⁷. As in the main text, we name them as the “polar SQUID”, which mimics the term “corner SQUID”⁹ for d -wave-YBCO phase-sensitive measurement. When the direction of the coupling is not reversed, we adopt the name “edge SQUID”⁹, according to the similar setup for d -wave-YBCO measurement.



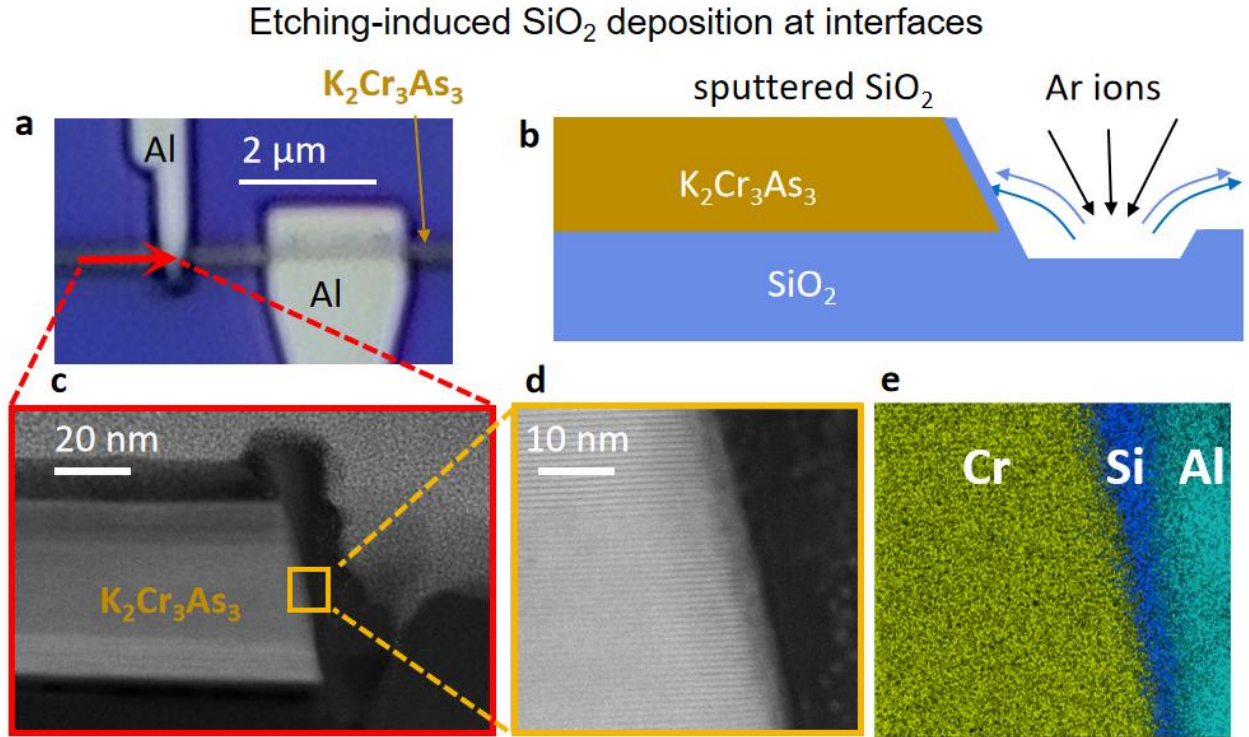
Supplementary Fig. 1. Realistic “quasi-polar SQUIDs” in p -wave superconductivity PSM: **a**, polar-SQUID for detecting p -wave superconductivity in $\text{K}_2\text{Cr}_3\text{As}_3$. The vector of the supercurrent across the Al- $\text{K}_2\text{Cr}_3\text{As}_3$ interfaces rotates by 180° and should introduce a π -phase in the SQUID supercurrent. **b**, edge SQUID where the vector of the supercurrent across the Al- $\text{K}_2\text{Cr}_3\text{As}_3$ interfaces rotates by 0° and introduces only 0-phase in the supercurrent. **c-e**, p -wave quasi-polar SQUIDs with partially (**e**) or fully etched facets which is non-vertical (**c**) or rough with microfacets (**d**). Due to different facets involved in the supercurrent, both 0- and π -phase should be present in such setups. For **c,d,e**, the details, such as the SiO_2 barrier which will be discussed later, is not concluded here.

The theoretical proposal⁷ considers only the π -phase contribution to the polar SQUID, and only 0-phase contribution to the edge SQUID. However, in realistic devices, both 0- and π -phases are present and we use the device configuration in Supplementary Fig. 1e for most of our devices because of the following reasons:

First, the experimental SQUIDs, even if designed strictly as the theoretical polar SQUID in Supplementary Fig.1a, will correspond to several more realistic configurations such as Supplementary Figs. 1c-d. One typical situation is the interfaces between *s*-wave and *p*-wave superconductors are not perfectly straight (sketched in Supplementary Fig. 1c) due to the etching direction as proved in Supplementary Fig. 2c. Another is the interface is not atomically-smooth and with microfacets (sketched in Supplementary Fig. 1d and shown in Supplementary Fig. 2d), which also appear in other systems such as the YBCO grain boundary with a typical length scale of $\sim 1\text{nm}$ ^{10,11}. In such realistic devices, supercurrent flowing through all the possible facets than just along *c*-axis also provides the admixture of both 0- and π -phases (similar situation was discussed also in *d*-wave PSM⁸⁻¹¹). We term them as the “quasi-polar SQUIDs”. Therefore, they are in principle similar to the design in Supplementary Fig. 1e which is with partially etched facets.

Second, because of non-uniform shape of $\text{K}_2\text{Cr}_3\text{As}_3$ and anisotropic etching, it is very challenging to just etch through $\text{K}_2\text{Cr}_3\text{As}_3$ without further etching the SiO_2 substrate underneath, required by the ideal polar SQUID. By taking the TEM, we indeed observe a thin layer of sputtered dust of SiO_2 onto the etched surfaces of the $\text{K}_2\text{Cr}_3\text{As}_3$ (Supplementary Figs. 2b,e¹²). Such unintentional SiO_2 layer is undesirable for the PSM because: a. Different parity of the order parameters between the *s*-wave and *p*-wave superconductors requires twice the *s*-*p*-*s* reflections in comparison to the single reflection in the conventional *s*-*i*-*s* Josephson junctions¹³, that is the coupling between *s*-wave and *p*-wave pairing is related to t^4 (*t* is the transmission of the interface),

instead of t^2 for the s - s Josephson coupling. Therefore, any sub-optimal interfaces will result in a rapid reduction of the s - p Josephson coupling. b. The weak s - p Josephson coupling will further reduce or even remove the π -phase contribution, making it insufficient to cancel the first harmonic beyond the ballistic junction limit $g = |I_2/I_1| = 1/2$ and form the ϕ -state¹⁴. Therefore, as shown in details in the zoomed-in figure of the main text Fig. 1c, the quasi-polar SQUID with partially etched $\text{K}_2\text{Cr}_3\text{As}_3$ can to some extent prevent the side-wall deposition of SiO_2 particularly on the c -facet, which is crucial for the p -wave PSM. Meanwhile, as discussed before, the quasi-polar SQUID with partially etched facets in Supplementary Fig. 1e is in principle the same as Supplementary Figs. 1c and d in view of the PSM which is still sensitive to the π -phase supercurrent in the 0 - π admixture. This justifies our adoption of such configuration (Supplementary Fig. 1e, the details are in Fig.1c of main text) for most of our devices.



Supplementary Fig. 2. Unintentional SiO_2 deposition in the fully etched quasi-polar SQUIDs:

a. optical image of the device showing direction of the TEM cut (red arrow). **b.** illustration of unintentional SiO_2 deposition at the $\text{K}_2\text{Cr}_3\text{As}_3$ interfaces, which is very normal during etching

process¹². **c.** TEM image of cross-section in the device showing the slant interface of Al and the fully etched $\text{K}_2\text{Cr}_3\text{As}_3$. **d.** zoomed-in TEM showing the non-vertical and amorphous interface with microfacets at the order of magnitudes of 1nm. **e.** EDS analysis showing SiO_2 deposition at the fully-etched interface.

Finally, we emphasize that the third contact (JJ_C in the main Fig. 1c) in the middle of $\text{K}_2\text{Cr}_3\text{As}_3$ is simply used for connecting the quasi-polar SQUID to the external circuit and does not participate in the PSM. Its introduction does not break the continuity of the $\text{K}_2\text{Cr}_3\text{As}_3$ crystal. Also in Supplementary Sec. 12, we explicitly demonstrate the JJ_C is in series with the SQUID whose supercurrent does not oscillate with magnetic field and is well separated with the SQUID supercurrent.

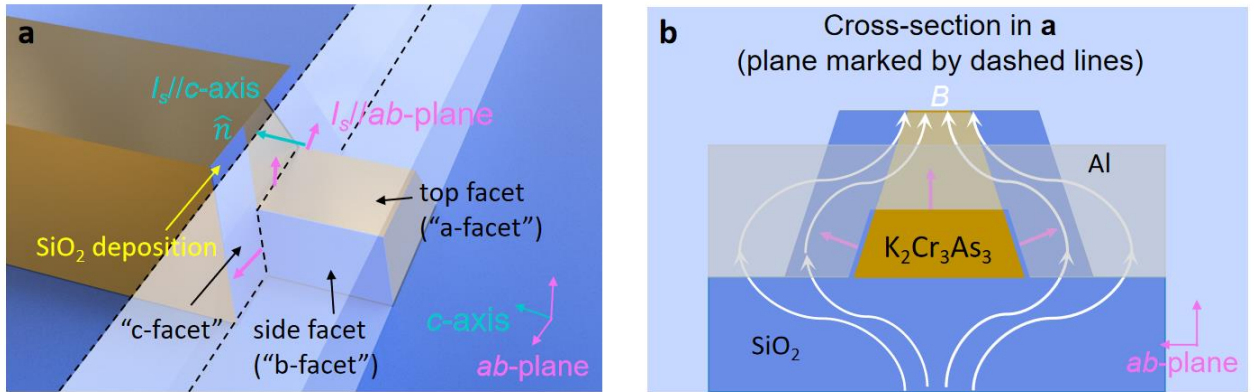
We would like to emphasize again that the experimental realization of PSM for *p*-wave superconductor is challenging, because of the possible complex phases in realistic materials and non-ideal situations rising from device nanofabrication. However, with the above reasons, it is justified that the adoption of the partially etched quasi-polar SQUID design in our measurement is a theoretically valid and experimentally viable phase-sensitive test for the π -phase supercurrent of *p*-wave superconductivity. Even supercurrents flowing along both *c*-axis and *a/b*-axis are included in this quasi-polar SQUID, it might still be more sensitive to that of *c*-axis, as will be discussed in the following Supplementary Sec.5.

5 Possible π -phase supercurrent in c-axis

Our data further support that the π -phase supercurrent might be mainly from c-axis (notably, without attempting to exclude there is also π -phase contribution from a/b-axis). The reasons are as follows:

1. In such configuration, the phase of the supercurrent is less sensitive to p -wave pairing along a/b-axis than c-axis: Supplementary Fig. 3a illustrates a single junction of the partially etched quasi-polar SQUID. Following Fig. 1c of the main text, we here call the facets pointed out in by the black arrows as “a/b/c-facets”, respectively (Supplementary Fig. 3a). It shows that the supercurrent flowing in the ab-plane indeed rotates by 180° with respect of b-axis (pink arrows) and thus may detect π -phase supercurrent if p -wave pairing exists in the b-axis. However, since there are two such junctions in the quasi-polar SQUID, the π -phase contribution at each junction gives a 2π -phase (or 0-phase) supercurrent in the whole SQUID. Therefore, the whole SQUID can only show 0-phase supercurrent, no matter whether the b-axis contains p -wave superconductivity or not. Besides, as sketched in Supplementary Fig. 3a, the interfaces between the Al-“b-facets” include an unintentionally sputtered SiO_2 layer (yellow arrow in Supplementary Fig. 3a) even in the partially-etched case, which also reduces the Josephson coupling in the b-axis direction. In addition, this device configuration does not rotate by 180° with respect of a-axis, and thus is not related to the p -wave superconducting pairing along a-axis. Therefore, our partially-etched quasi-polar SQUID is insensitive to p -wave superconductivity in a/b-axis. On the other hand, light blue arrows in Supplementary Fig. 3a shows a non-rotating, stable n-vector for the supercurrent flowing in the c-axis. Such vector rotates by 180° throughout the two junctions in the SQUID (main text Fig. 1c) thus providing exactly the condition required by p -wave PSM in the c-axis⁷. Therefore, our design is more sensitive to π -phase supercurrent originating from the p -wave superconductivity in c-axis.

2. Although the supercurrent may flow across different interfaces (Al-a/b/c axis), their tunability by the magnetic field is different. As shown by Fig. 3a and Supplementary Fig. 3b, due to the Meissner effect, the field is distorted in the ab-plane. Therefore, the I_s parallel to the ab-plane (pink arrows) is not much exposed to the field and thus cannot be efficiently controlled by it. On the contrary, the supercurrent flowing across the Al-“c-facet” interface (light blue arrows in Supplementary Fig. 3a) is less affected by the screening and could be effectively modulated by the magnet field. It is clearly shown that in Fig. 3 of the main text, the π -phase supercurrent component is highly tunable by the magnetic field, and thus should correspond mainly to the supercurrent flowing across in c-axis, similar to the modulated I_c oscillation pattern of SQUID by flux pinning through YBCO grain boundary junctions^{10,11}.

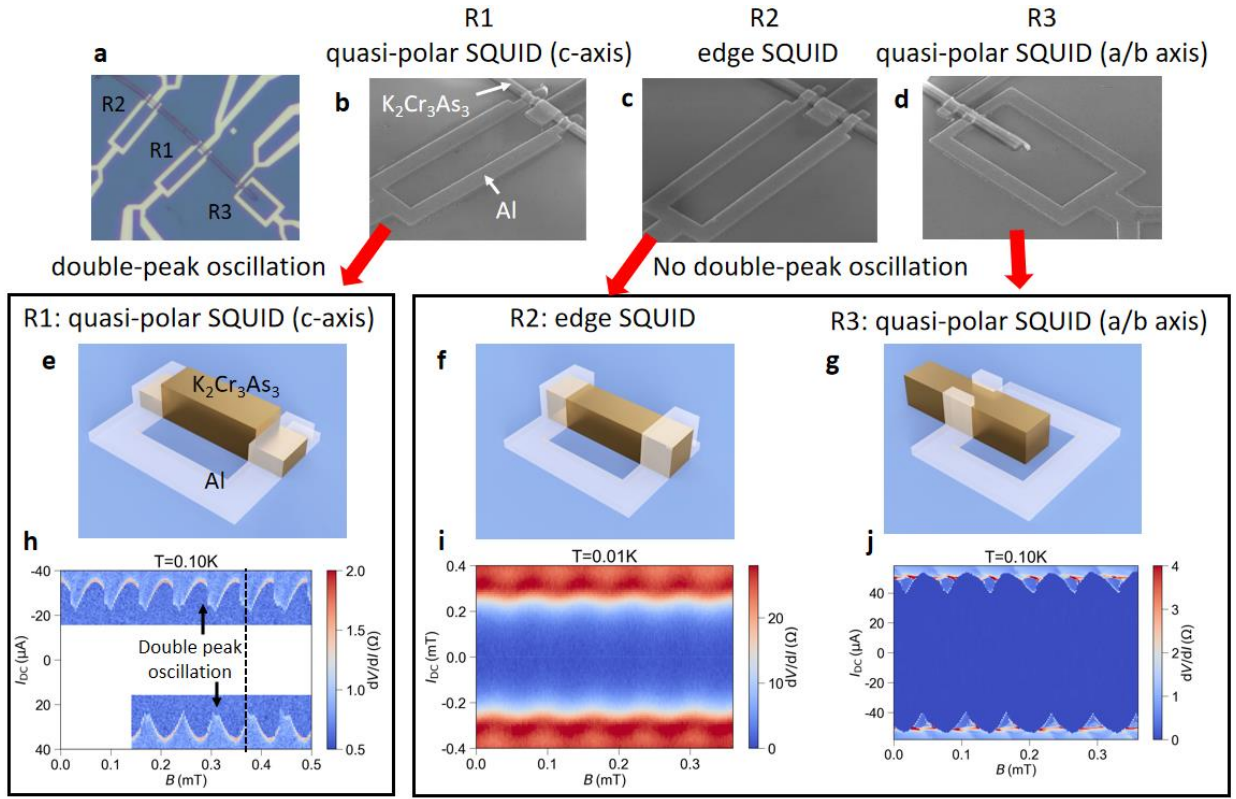


Supplementary Fig. 3. Models illustrating the field distortion and non-ideal interfaces at a Al-K₂Cr₃As₃ junction: **a**, 3D model zooming in to a single junction area of the partially-etched quasi-polar SQUID. The facets pointed out by the black arrows are defined as “a/b/c-facet”. SiO₂ also partially deposited (yellow arrow) on the interfaces even in the partially-etched quasi-polar SQUIDs, though not entirely as in the fully-etched case in Supplementary Fig. 2b. Supercurrent at the Al-K₂Cr₃As₃ interfaces has the component in c-axis with a stable n-vector (light blue arrows) and components in the ab-plane with rotating n-vector (pink arrows). **b**, 2D cross-section at the plane marked by the dashed lines in **a**. The distorted magnetic field lines penetrates between c-

facet of $\text{K}_2\text{Cr}_3\text{As}_3$ and Al film in the penetration length, but wraps around the remaining $\text{K}_2\text{Cr}_3\text{As}_3$ section. I_s //ab-plane (pink arrows) is not efficiently exposed to B due to Meissner effect. As a contrast, I_s //c-axis (blue arrows in **a**) could be modulated by B .

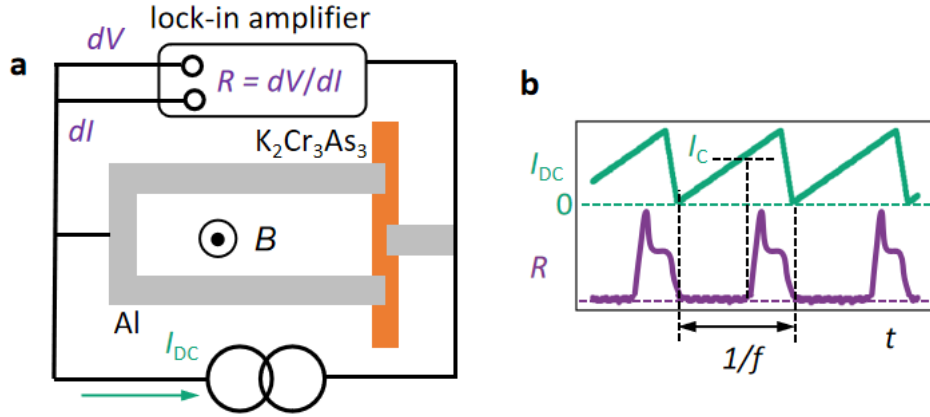
3. We also measured some devices where $\text{K}_2\text{Cr}_3\text{As}_3$ is completely etched and the JJs only connect to c-axis (as Supplementary Fig. 1c,d). As shown in later in Device E in Supplementary Figs. 12e, f, we observe there the double-peak oscillation characteristic to the ϕ junction, thus further demonstrating the presence of π -phase components in supercurrent flowing in c-axis. The weak double-peak oscillation occurred at higher field is also consistent with the reduced s-p coupling by unintentional SiO_2 deposition at the interface in the fully-etched devices.

4. In Supplementary Fig. 4, we also fabricate different SQUIDs on the same $\text{K}_2\text{Cr}_3\text{As}_3$, which are one edge SQUID (R2) and two quasi-polar SQUIDs along c-axis (R1) and a/b-axis (R3) respectively. We only observe the ϕ -state with double-peak oscillation in R1 (Supplementary Fig. 4h) around zero field, which means the π -phase from c-axis is more predominating than that from the a/b-axis. We note that here we do not attempt to exclude the possible π -phase contribution from other two SQUIDs in other situation, for example, at higher magnetic field or lower temperature. Our data simply indicate that the π -phase along c-axis is much stronger than other two cases.



Supplementary Fig. 4. Comparison between quasi-polar SQUID in the c-axis (R1) and a/b-axis (R3) and the edge SQUID (R2): **a**, optical image showing three devices fabricated on the same $\text{K}_2\text{Cr}_3\text{As}_3$ crystal. **b-d**, SEM images of the three devices. In R2 the $\text{K}_2\text{Cr}_3\text{As}_3$ crystal is very lightly etched so that the surface area in the “c-facets” (defined in Supplementary Fig. 3a) is much smaller than that of R1 which is etched heavily. In R3, the etching recipe is the same as that of R1, but along “b-facets” instead of “c-facets” (defined in Supplementary Fig. 3a). **e, h**, schematic of R1 and the measured $I_c(B)$ oscillation of the supercurrent showing double-peak feature (black arrow) and thus high π -phase component. $T = 100$ mK. The dashed vertical line marks the same B range as to **i** and **j**. **f, i**, schematic of R2 and the measured $I_c(B)$ showing the normal 2π -periodic oscillation and no double-peak feature. $T = 10$ mK. **g, j**, schematic of R3 and $I_c(B)$ showing no double-peak oscillation. $T = 100$ mK. The details of the devices, such as the SiO_2 barrier at the interface, are not included in the schematics in **e,f,g**.

6 Fast counter measurement of $I_c(B)$ in Figure 3

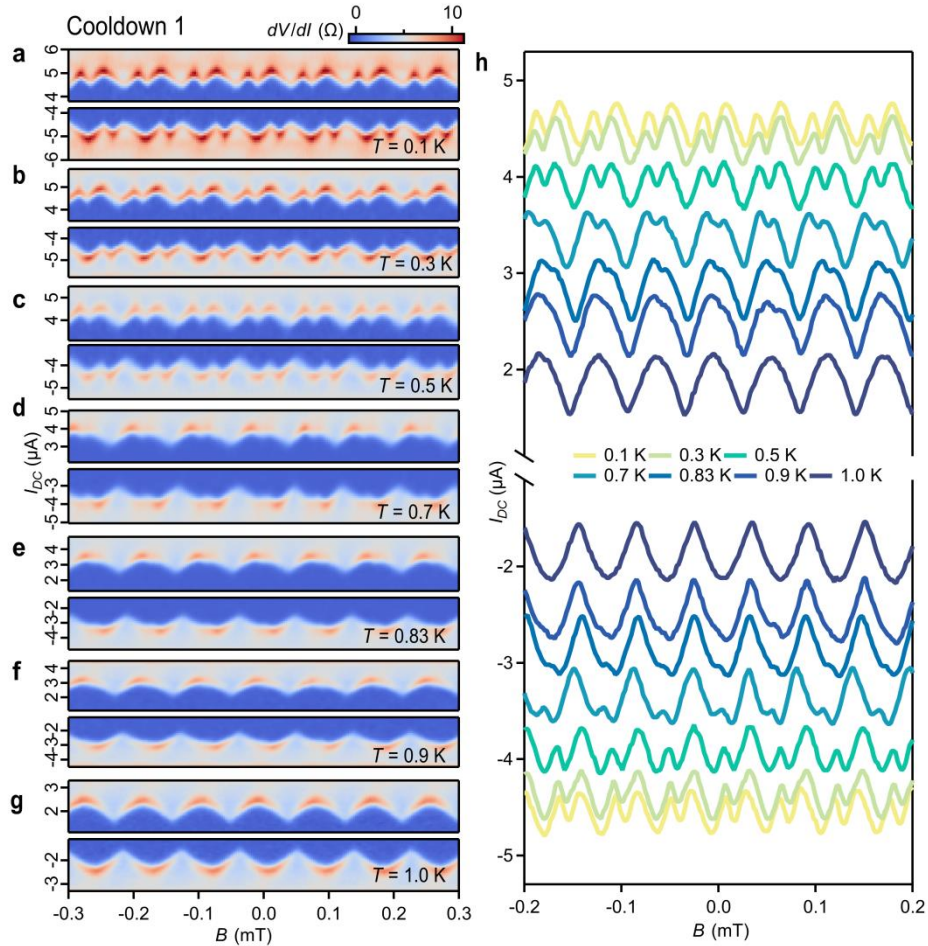


Supplementary Fig. 5. Schematic showing fast-pulse measurement setup: a, Setup involving a lock-in amplifier and a fast pulse generator providing the triangular wave of $I_{DC}(t)$ (green waveform in **b**). **b**, Time-domain signals for I_{DC} and R with frequency f . I_c is determined at t where R becomes non-zero.

The many oscillations over wide range of B in Fig. 3 of the main text are obtained by the fast counter measurement technique commonly adopted in SQUID characterization^{15,16}. In such method, I_{DC} is ramped linearly and continuously from 0 to above I_c , and the dc voltage of the SQUID is monitored. When $I_{DC} = I_c$, the voltage will jump from 0 (the superconducting state) to the finite value (the normal state) which triggers a counting event of a digital counter. The time interval between $I_{DC} = 0$ and $I_{DC} = I_c$ obtained by the counter thus provides a fast measurement of I_c over a wide range of B . The pulse frequency f is much smaller than the cut-off frequency of the lock-in amplifier so that R is not distorted.

7 Extended data for Figs. 2-3

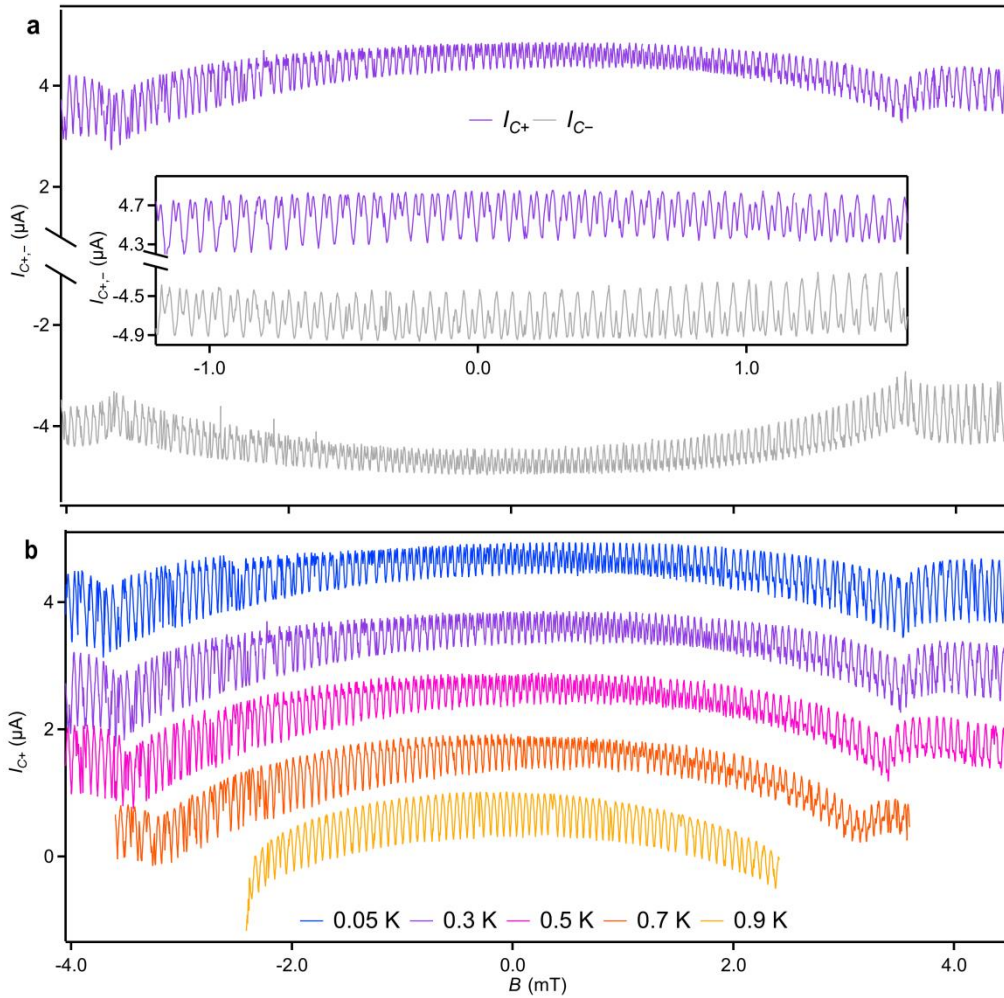
Supplementary Figure 6 completes the series of $dV/dI(I_{DC}, B)$ of Figs. 2a-d of the main text with more data points in temperature. The extracted $I_c(B)$ in Supplementary Fig. 6h shows the double-peak features at low T and gradual evolution to single peak feature for $T > 0.8$ K, similar to Fig. 2e of the main text. The data is taken in a separate thermal cycle (Cooldown 1) where the sample is heated above T_c of $K_2Cr_3As_3$, and the reproducibility of the main features of $I_c(B)$ demonstrates the robustness of the ϕ -JJ state in the system.



Supplementary Fig. 6. Extended data for Figs. 2a-d of the main text with more temperature points. a-g, $dV/dI(I_{DC}, B)$ with $T = 0.1, 0.3, 0.5, 0.7, 0.83, 0.9, 1.0$ K. h, Extracted $I_{c+,-}$ versus B for all the temperatures. a, c, e, g are the same as the main text Figs.

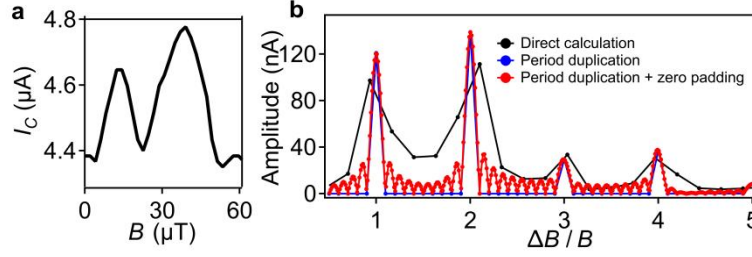
2a-d (Cooldown 1)

Supplementary Figure 7a shows the similar data as Fig. 3a of the main text measured over a wide range of B at $T = 0.3$ K, again showing a transition where the double-peak oscillation is the clearest. Supplementary Figure 7b also shows the wide sweeps at several temperatures.



Supplementary Fig. 7. Extended data for Fig. 3a with more temperature points. a, Positive and negative critical current $I_{c+,-}(B)$ at $T = 0.3$ K, again showing double-to-single peak transition, similar to the 0.1 K data in Fig. 3a of the main text. Inset: the zoomed-in plot across the transition region. **b,** $I_{c+}(B)$ for all other measured temperatures $T = 0.05, 0.3, 0.5, 0.7$ and 0.9 K.

8 Fourier analysis of $I_c(B)$



Supplementary Fig. 8. Fourier analysis for $I_c(B)$: **a**, $I_c(B)$ data. **b**, FFT amplitude spectrum of the data in **a**, calculated in three methods: 1. direct calculation (black), 2. period duplication (blue), 3. period duplication and zero padding (red, also the one used in the main text). ΔB is the length of the x -axis in **a**.

The measured $I_c(B)$ in the main Fig. 3 is reproduced in Supplementary Fig. 8, and the amplitude of the Fourier spectrum is numerically calculated by the fast Fourier transform (FFT) algorithm. The result from the direct calculation is plotted in Supplementary Fig. 8b (black dots). The amplitude is enhanced at $n = \Delta B/B = 1$ and 2, indicating the strong first and second harmonic of $I_c(B)$ shown in Supplementary Fig. 8a. Adopting the common practices for Fourier analysis¹⁷, duplicating the data by several periods further sharpens the harmonic peaks (blue dot). Appending a string of zeros (“zero-padding”) to the duplicated data also enhances the frequency resolution of the FFT (red dot). In the main figures, we consistently use the method of period duplication and zero padding to calculate the Fourier spectrum and to accurately extract the first and second harmonics.

9 Fitting of $I_c(B)$

Supplementary Figures. 9a-b show the original 2D plots used to extract $I_c(B)$ in the main text Fig. 2e. As described in the main text equation (1), the SQUID in the φ -JJ state can be modeled as the two Josephson junctions in parallel (noted as JJ_A and JJ_B), each with the CPR $I(\varphi) = I_1 \sin(\varphi) - I_2 \sin(2\varphi)$. Since in the measurement the averaged I_c ($\sim 4 \mu\text{A}$) is around ten times higher than its flux variation ($\sim 0.4 \mu\text{A}$), it is justified to simplify the CPR of the strong junction (say JJ_B) as purely sinusoidal, without affecting the shape of $I_c(B)$. The inductance of the SQUID is calibrated using the data at high temperature $T = 1.0$ and 1.1 K, where we neglect the second harmonic. This results in $L = 88$ pH (or $\beta = LI_c/\Phi_0 \approx 0.3$). Such value is higher than expected for Al contacts¹⁸ but possibly originates from the kinetic inductance¹⁹ of K₂Cr₃As₃.

By fixing L , the measured $I_c(B)$ in Supplementary Figures. 9a-b can be fitted by the equation (2) in the main text. In order to increase the accuracy of the fitting, we introduce two fitting parameters: a relative phase shift $\Delta\varphi_2$ between the first and the second harmonics and an extra phase $\Delta\varphi_S$ in the SQUID loop, which are present possibly due to the spontaneous current^{7,20-26}. Therefore, the model for our system can be written as^{9,27-29}:

$$I_c(\Phi) = \max_{\varphi_A} \{I_A(\varphi_A) + I_B(\varphi_B)\} \quad (\text{S2A})$$

$$I_A(\varphi_A) = I_{A1} \sin(\varphi_A) - I_{A2} \sin(2\varphi_A + \Delta\varphi_2) \quad (\text{S2B})$$

$$I_B(\varphi_B) = I_{B1} \sin(\varphi_B) \quad (\text{S3C})$$

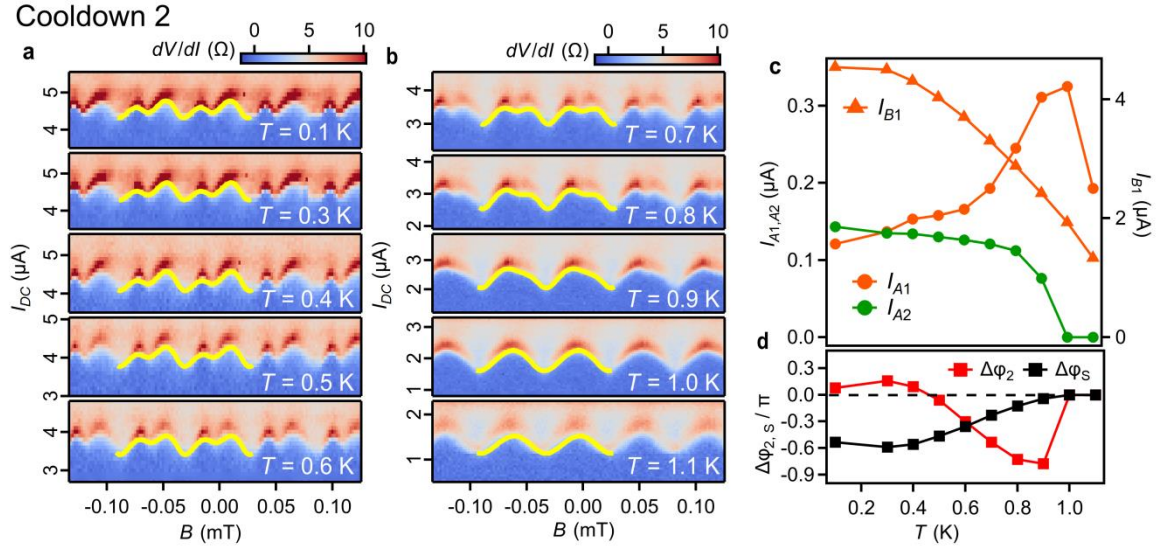
$$\varphi_A - \varphi_B + 2\pi L[I_A(\varphi_A) - I_B(\varphi_B)]/\Phi_0 = 2\pi\Phi/\Phi_0 + \Delta\varphi_S \quad (\text{S2D})$$

where L is the inductance in the SQUID loop.

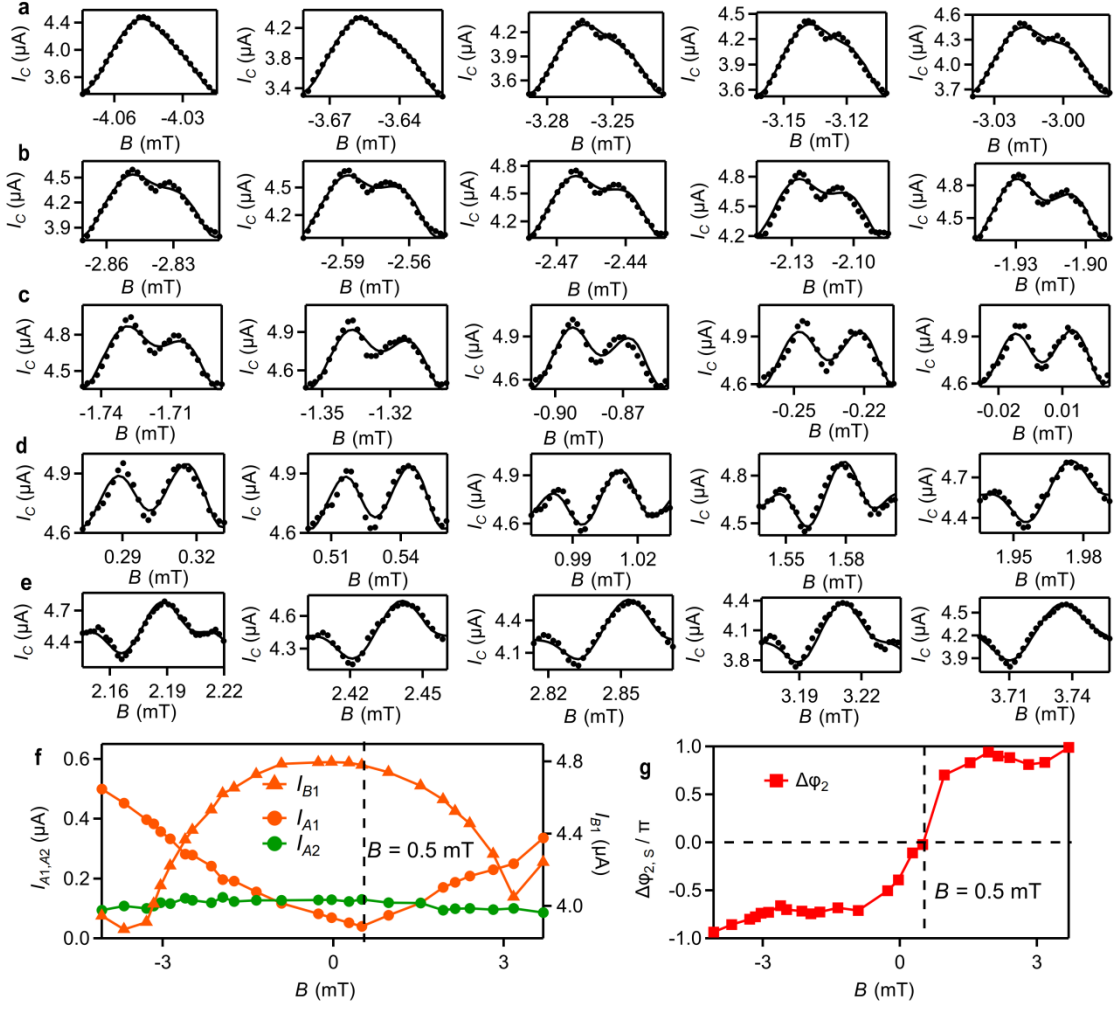
Using Supplementary Equation (S2), we have achieved reasonably good agreement with the data for all temperature points, as demonstrated by overlapping the fitted $I_c(B)$ (yellow) on the 2D plots (Supplementary Figs. 9a,b). The fitting parameters I_{A1} and I_{A2} are reproduced from Fig. 2g in Supplementary Fig. 9c. We emphasize that the other fitting parameters $\Delta\varphi_2$ and $\Delta\varphi_S$ (Supplementary Fig. 9d), introduced to increase the accuracy of the fitting, do not affect the magnitudes of the first and second harmonics of the JJs. Indeed, as demonstrated in Fig. 2h, the FFT, which is insensitive to $\Delta\varphi_2$ and $\Delta\varphi_S$ but directly captures the amplitudes of the first and

second harmonics, still gives the almost identical results to the fitting. Therefore, it demonstrates beyond doubt that at low temperatures $g > 1/2$ and the SQUID is in the φ -JJ state.

Similarly, Supplementary Figures 10a-e reproduce all the segments of $I_c(B)$ used in Fig. 3d-f taken at the fixed $T = 0.1$ K but different B . By fitting each segment to Supplementary Equation (S2), we obtain the fitting parameters shown in Supplementary Fig. 10f (same as Fig. 3e) and 10g. Again, although $\Delta\varphi_2$ (Supplementary Fig. 10g) is needed to increase the accuracy of the fitting, its inclusion does not alter the harmonic amplitudes I_{A1} and I_{A2} which are almost identical to the FFT in Fig. 3d.



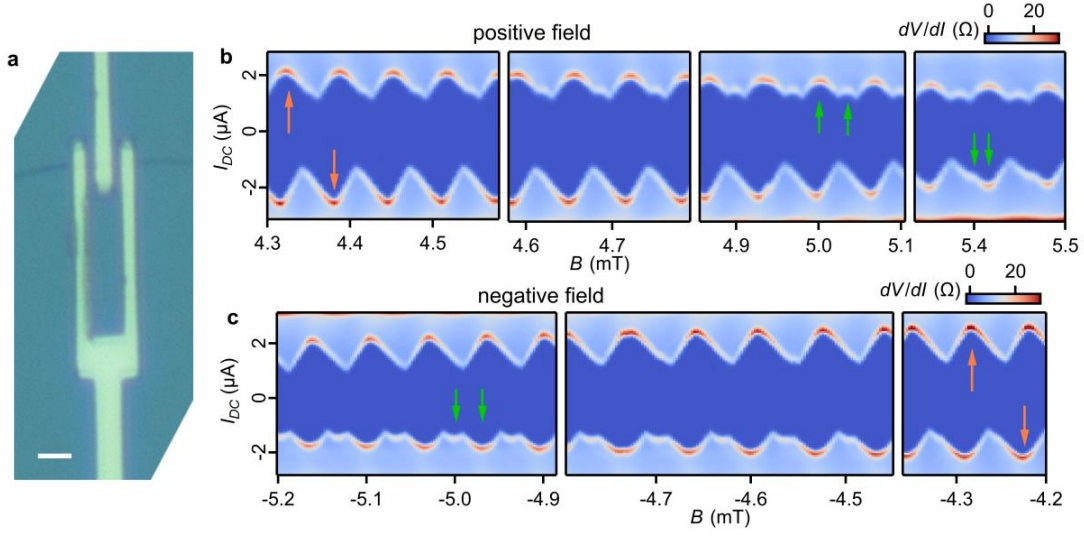
Supplementary Fig. 9. Flux-dependent critical current for Cooldown 2: **a-b**, $dV/dI(I_{DC}, B)$ at $T = 0.1, 0.3, 0.4, 0.5, 0.6, 0.7, 0.8, 0.9, 1.0$ and 1.1 K are the original 2D plots used to extract $I_c(B)$ in Fig. 2e. The fitting results of $I_c(B)$ are overlapped for all the figures. **c**, Fitting parameters (the two harmonics of JJ_A ($I_{A1,2}$) and the first harmonic of JJ_B (I_{B1})) versus T . The data is the same as Fig. 2g. **d**, Fitting parameters (the relative phase shift between the two harmonics of JJ_A ($\Delta\phi_2$) and the extra phase shift between JJ_A and JJ_B possibly due to the self-generated flux ($\Delta\phi_s$)) versus T .



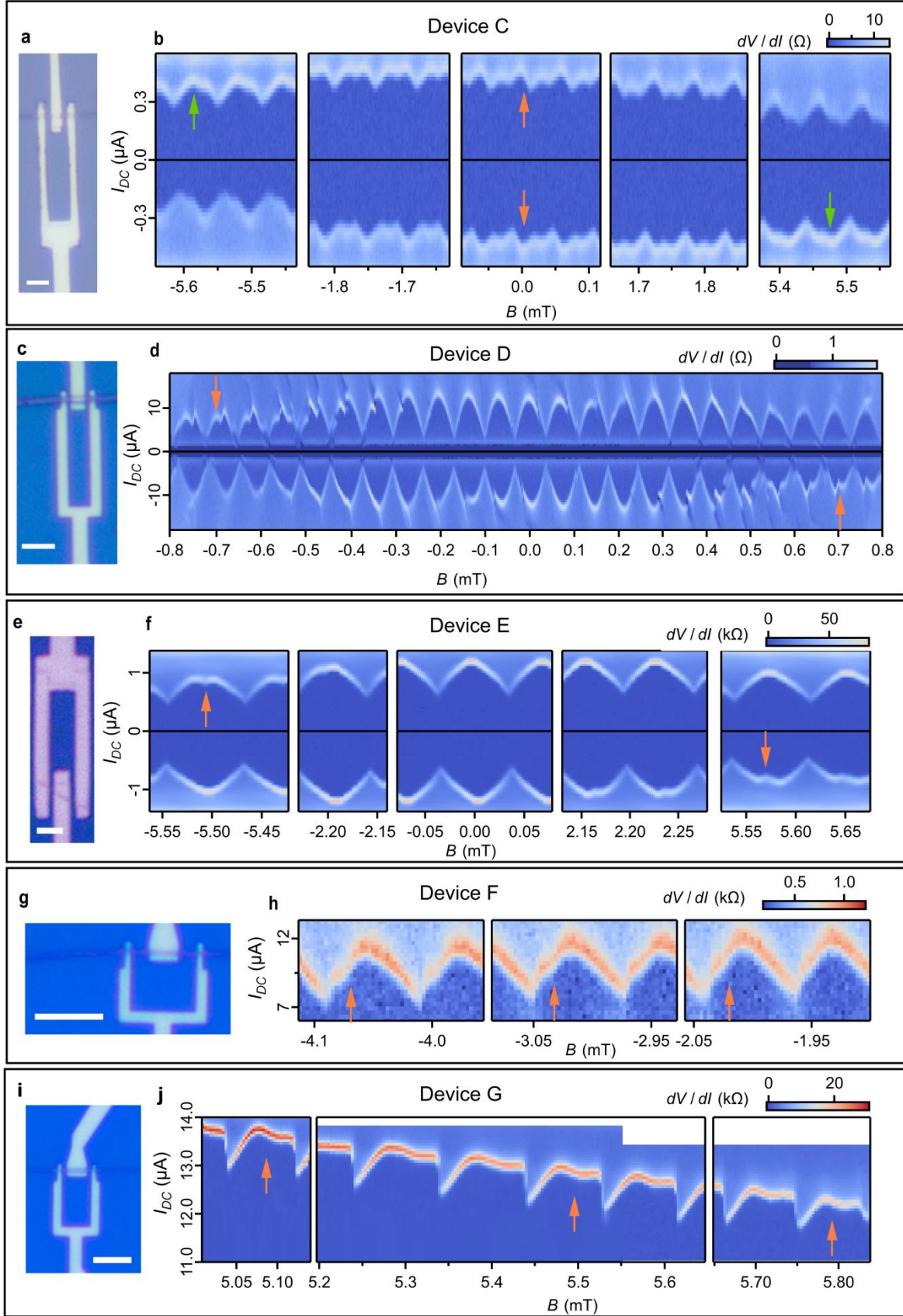
Supplementary Fig. 10. Extended data for Fig. 3: **a-e**, All the measured $I_c(B)$ segments at different B (dots) with the fitting curves (solid lines) used for Fig. 3e in the main text. **f**, The fitting parameters $I_{A1, 2}$ and I_{B1} versus B reproduced from Fig. 3e. Each point corresponds to a $I_c(B)$ panel in **a-e**. $g = |I_{A2}/I_{A1}|$ is maximal at $B = 0.5$ mT. **g**, $\Delta\phi_2$ versus B , $\Delta\phi_2(B)$ is roughly an odd function with respect to $B = 0.5$ mT

10 More devices with and without quasi-double-periodic features

We first show other similarly fabricated devices which also exhibit the quasi-double-periodic structure in the phase-sensitive measurement. The optical image of the SQUID device (Device B) with similar geometry is included in Supplementary Fig. 11a. The wider range $I_c(B)$ is plotted in Supplementary Fig. 11b, where the quasi-double-periodic features in the SQUID oscillations emerge in the positive I_{DC} for $B \sim 5$ mT. Similar to Fig. 3, the oscillation pattern is always point symmetric with respect to zero field¹⁰ and such quasi-double-periodic oscillations also appear in the negative I_{DC} for $B \sim -5$ mT (Supplementary Fig. 11c). The typical segments of $I_c(B)$ (positive current for $B \sim 5$ mT and negative current for $B \sim -5$ mT) can also be characterized by FFT, giving $g = F_2/F_1 = 0.72 > 0.5$. Similarly, Device C also shows clear quasi-double-periodic oscillations for both negative and positive I_{DC} near zero field (Supplementary Figs. 12a, b). Device D where I_c of the SQUID is higher than that of the contact junction JJ_C outside the SQUID, the quasi-double-periodic oscillation is also observed ~ 0.7 mT (Supplementary Figs. 12c, d). Finally, Device E-G exhibit weaker double-periodic oscillations also at finite fields (Supplementary Figs. 12e-j). Devices A-G thus demonstrate the reproducibility of the ϕ -state in Al-K₂Cr₃As₃ quasi-polar SQUIDs.



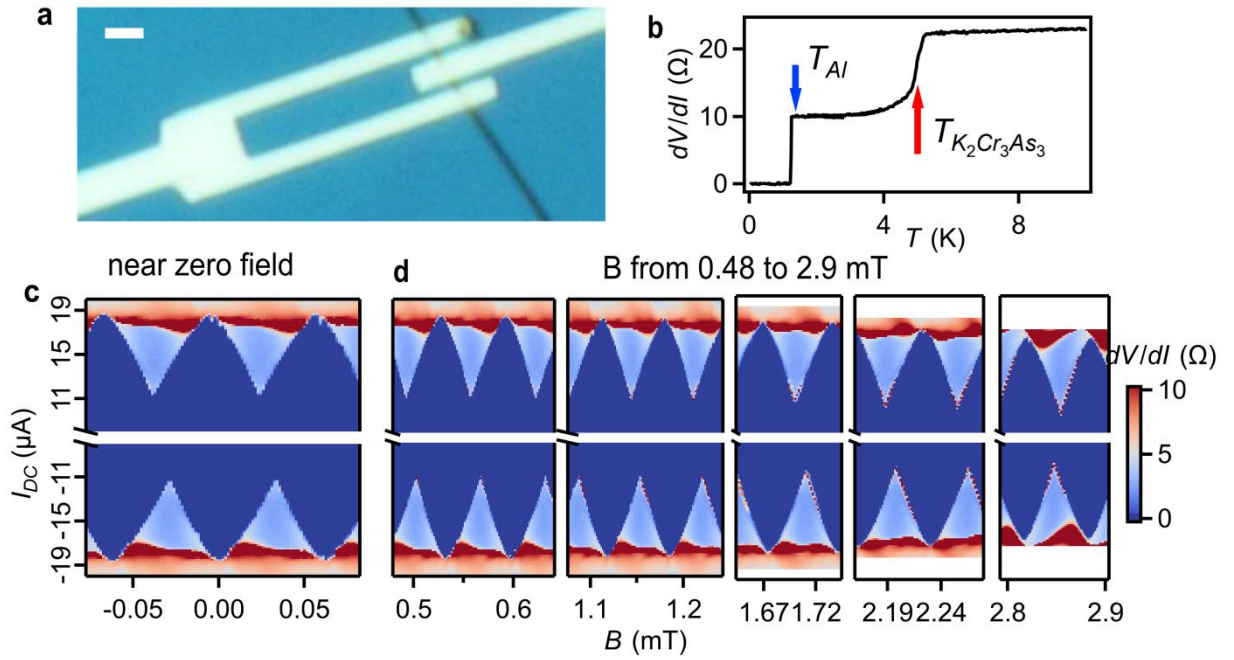
Supplementary Fig. 11. Device B showing single- to quasi-double-periodic oscillations: **a**, Optical image. Scale bar: 2 μm . **b**, $dV/dI(I_{\text{DC}}, B)$ measured at $T = 96$ mK, showing a clear transition from the single- (orange arrows) to quasi-double-periodic (green arrows) oscillations in the positive I_{DC} for positive fields. **c**, Same as **b** showing single- to quasi-double-periodic transition in the negative I_{DC} for the negative fields. The FFT at the quasi-double-periodic oscillations (green arrows) gives $g = F_2/F_1 = 0.72 > 1/2$.



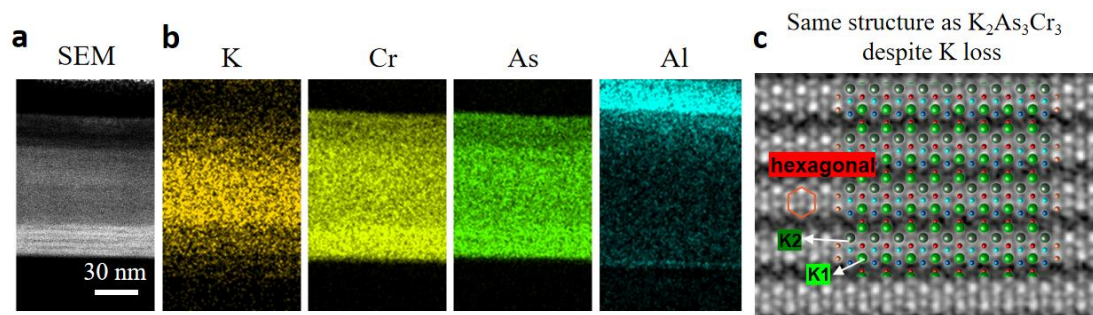
Supplementary Fig. 12: Devices C-G showing quasi-double-periodic oscillations: Device C: a,

Optical image. Scale bar: 5 μm . **b**, $dV/dI(I_{\text{DC}}, B)$ measured at $T = 10$ mK, showing a clear quasi-double-periodic oscillations (orange arrows) near zero field. $I_{\text{C}}(B)$ patterns (green arrows) at higher fields obey the Onsager relation. **Device D:** **c**, Optical image. Scale bar: 5 μm . **d**, $dV/dI(I_{\text{DC}}, B)$ measured at $T = 1.15$ K, showing a weak double-peak oscillations (orange arrows) above ~ 0.7 mT. I_{c} of the SQUID is higher than that of JJ_{C} . **Device E:** **e**, Optical image. Scale bar: 5 μm . **f**, $dV/dI(I_{\text{DC}}, B)$ measured at $T = 10$ mK, showing a weak double-peak oscillations (orange arrows) above ~ 5 mT. **Device F:** **g**, Optical image. Scale bar: 5 μm . **h**, $dV/dI(I_{\text{DC}}, B)$ measured at $T = 10$ mK, showing a weak double-peak oscillations (orange arrows) more negative than ~ -2 mT. I_{c} of the SQUID is higher than that of JJ_{C} . **Device G:** **i**, Optical image. Scale bar: 5 μm . **j**, $dV/dI(I_{\text{DC}}, B)$ measured at $T = 10$ mK, showing a weak double-peak oscillations (orange arrows) higher than ~ 5 mT.

Meanwhile, for other devices fabricated via nominally the same process, no quasi-double-periodic oscillations are observed. Supplementary Figures 13a-b shows similar device (Device F1) geometry and $dV/dI(T)$ with similar superconducting transition temperatures. However, for wide range of field, no quasi-double-periodic oscillation is visible in either direction of I_{DC} (Supplementary Figs. 13c-d).



Supplementary Fig. 13. Device F1 showing only single-periodic oscillations: **a**, Optical image of the SQUID. Scale bar: 2 μm . **b**, Differential resistance dV/dI versus T . **c**, dV/dI versus I_{DC} and B near zero field. The critical current I_c shows only single-periodic oscillations. **d**, dV/dI versus I_{DC} and B for higher field.



Supplementary Fig. 14. EDS analysis of a section of stripe without double-periodic oscillations: Scale bar: 30 nm. **a.** The first image is the SEM taken simultaneously. **b.** The stripe is covered with a protection layer of AlO_x (orange). Contrary to the clear-cut boundaries of Cr (bright yellow) and As (green) which coincide with the SEM image, K (dark yellow) is visibly lost possibly due to aging effect. **c.** TEM showing that the hexagonal lattice of K₂Cr₃As₃ is unchanged despite K loss.

Several other devices (F2-F5, not shown) with different loop areas and junction areas also show single-periodic oscillations up to the critical field of Al. We note that F1-F5 were not measured immediately after fabrication, as Devices A-E were. Indeed, a typical EDS measurement shown in Supplementary Figure 14 showing that the element K is partially lost over time, even all the devices are covered by a protection layer of AlO_x and are stored in the glovebox. Therefore, the conventional SQUID oscillation may be due to the gradual degradation of the stripe. Meanwhile, due to the different crystal dimensions, anisotropy etching, and the unintentional deposition of the SiO_2 and so on, the devices showing quasi-double-periodic oscillations or not (and thus ϕ -JJ state or not) might be due to the interface details, as well as different chemical potential, and thus the different coupling between the crystal and the s/p -wave superconductors^{5,6,30}. Supplementary Table 1 lists the average critical current \bar{I}_c and the half of the oscillation amplitude ΔI_c . $\eta = \Delta I_c / \bar{I}_c$ thus describes the detailed information of the SQUID³¹.

Devices	\bar{I}_c (μA)	ΔI_c (μA)	η (%)
A	4.5	0.3	6.7
B	1.4	0.2	14.3
C	0.38	0.048	12.5
D	8.0	4.5	56.2
E	0.76	0.27	35.5
F	9.29	1.77	19.1
G	0.33	12.04	2.8
F1	14.9	3.5	23.5

F2	3.1	0.9	29 .0
F3	1.2	0.8	66 .7
F4	1.9	1.0	52 .6
F5	3.4	1.1	32 .3

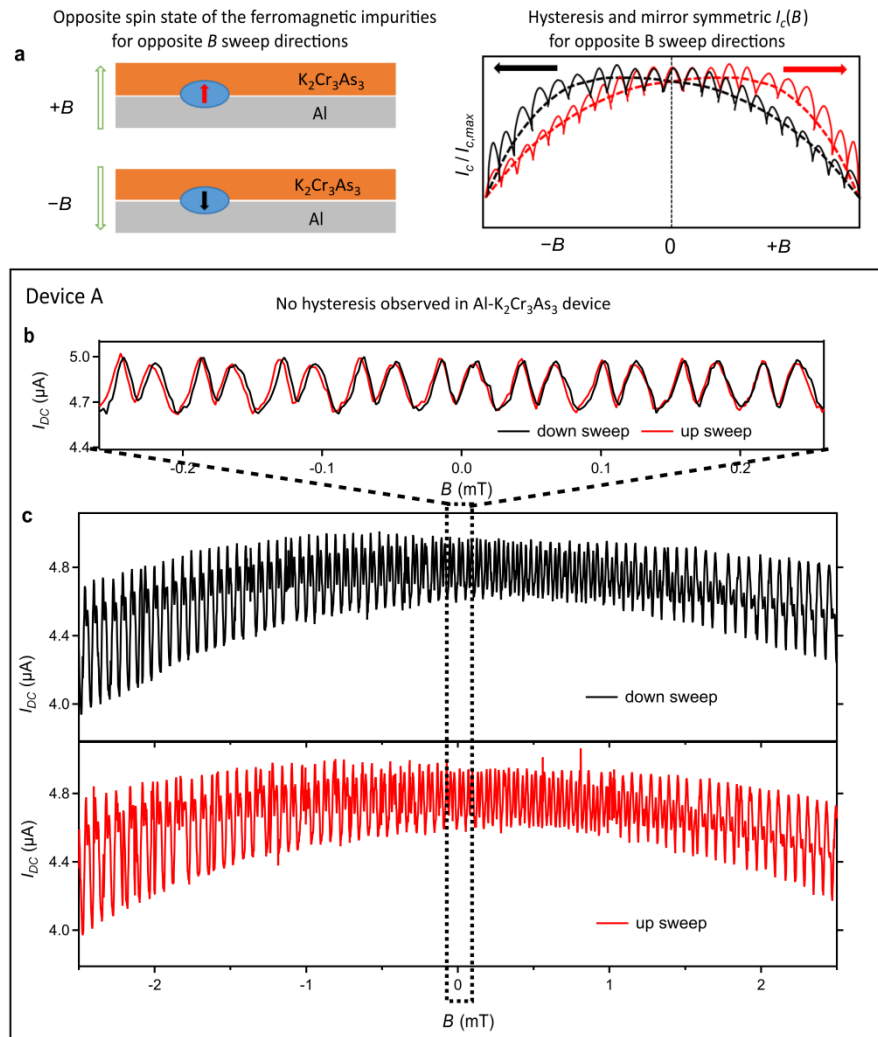
Supplementary Table 1. Summary of \bar{I}_c , ΔI_c and $\eta = \Delta I_c / \bar{I}_c$ for all devices. Devices A-G show quasi-double-periodic oscillations. Devices F1-5 show only single-periodic oscillations.

11 Ruling out residual ferromagnetism in Al-K₂Cr₃As₃ SQUIDs

It is possible that the observed ϕ -state is originated from the residual ferromagnetism of the sample instead of the p -wave superconductivity^{21,28}. Josephson devices with ferromagnetic components possess several general properties. First, they will show hysteretic behavior when B is stepped up or down³². Furthermore, different from the classical Fraunhofer pattern with $I_c(B) = I_c(-B)$, JJs may in some occasions display asymmetry between $I_c(B)$ and $I_c(-B)$, possibly due to mixture between conventional and unconventional superconductivity phases⁹, ferromagnetism³³⁻³⁵, and non-uniform supercurrent distribution or vortices³⁶⁻³⁷. As illustrated in Supplementary Fig. 15a, in the case of ferromagnetism, the asymmetric $I_c(B)$ will show a mirror-symmetric pattern with respect to $B = 0$ when B is stepped up or down across the coercive field³³⁻³⁵.

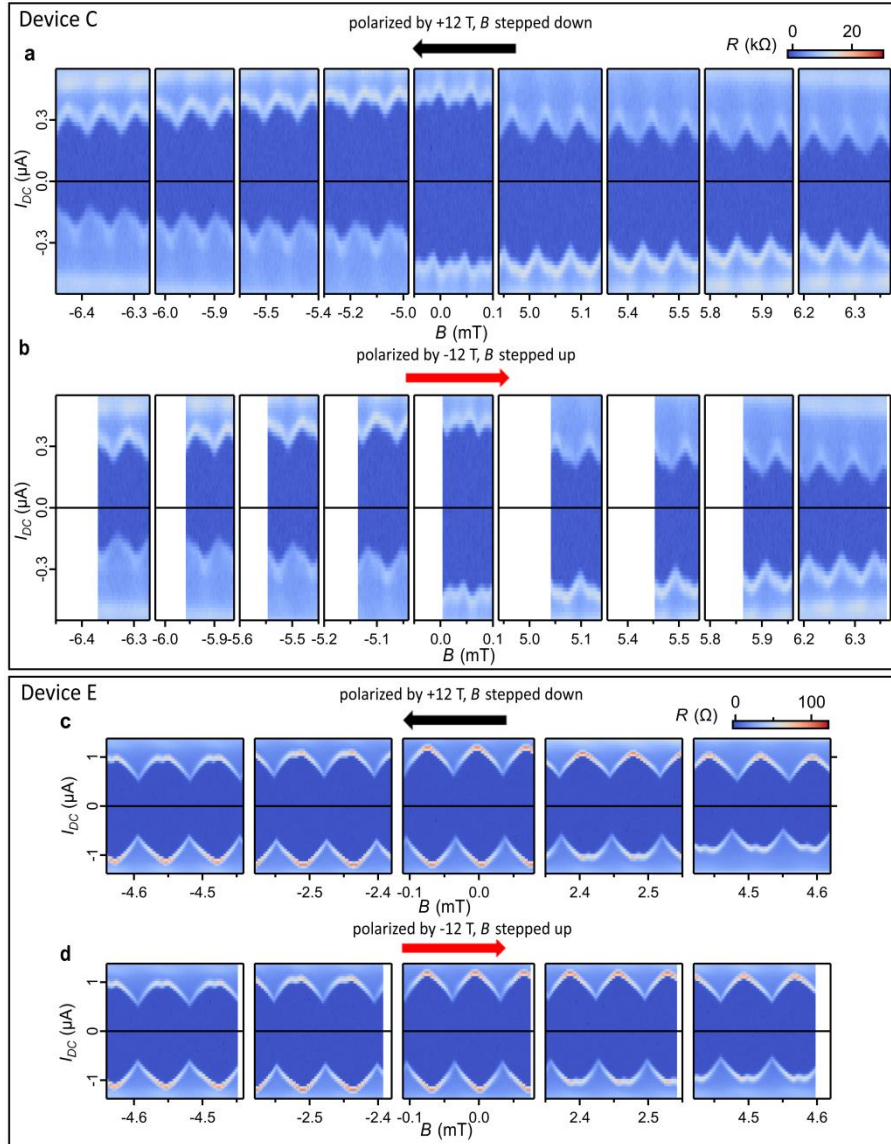
By checking these properties, we rule out ferromagnetism as the cause for the quasi-double periodic oscillation of $I_c(B)$ in our devices, for the following reasons: (1) As shown in Supplementary Fig. 15b when the field range is kept within ~ 0.3 mT, the detailed quasi-double periodic SQUID oscillation is identical with no hysteresis when B is stepped up or down. Apart from several glitches in the fast SQUID oscillations due to vortices, no hysteresis appears in the Fraunhofer envelop when we increase the range of sweep to 2.5 mT (Supplementary Fig. 15c). (2) $I_c(B)$ in Supplementary Fig. 15c is slightly asymmetric. However, no mirror symmetry explained before³³⁻³⁵ is present between the patterns with up-stepping and down-stepping B . (3) It remains possible that the ferromagnetic components have the coercive fields much higher than 2.5 mT. To exclude such possibility, we first apply the magnetic field of +12 T to another similar device Devices C and then measure $I_c(B)$ oscillations again around zero field after the strong field is withdrawn (similar to the low field measurement, B is stepped down after +12 T polarization, see Supplementary Fig. 16a). Then, similar $I_c(B)$ pattern is measured after applying -12 T, which also reproduces identical pattern (B is stepped up after -12 T polarization, Supplementary Fig. 16b). The robustness of the $I_c(B)$ pattern after applying ± 12 T are also reproduced in Device E (Supplementary Figs. 16c,d). Therefore, the absence of neither hysteresis nor mirror symmetric

pattern between up and down sweep with different strength of polarization field clearly shows that our data is drastically inconsistent with the ferromagnetic JJs, and thus we demonstrate beyond doubts that the observed ϕ -state is intrinsic to $\text{K}_2\text{Cr}_3\text{As}_3$ not related to ferromagnetism. We can also exclude the vortices as the source for the unconventional interference pattern by these three reasons, with an additional reason that we can reproduce the pattern after several cooling down processes with close-to-zero field.



Supplementary Fig. 15. Ruling out ferromagnetism by showing no hysteresis or mirror-symmetric $I_c(B)$ in Al-K₂Cr₃As₃ SQUIDS: **a**, Cartoons (left) showing two equivalent states for a Josephson junction with ferromagnetic components with opposite spin polarizations by applying opposite magnetic field. Example $I_c(B)$ (right) for the SQUID containing ferromagnetic

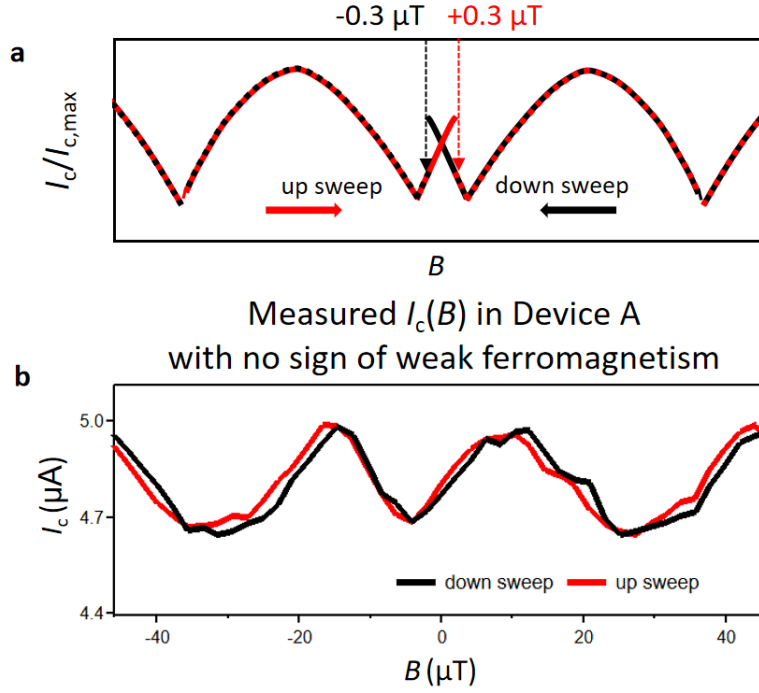
components in the opposite spin states, measured by stepping up (red) and down B (black). The Fraunhofer background (dashed lines) of the two $I_c(B)$ curves show hysteresis³² and are mirror-symmetric with each other with respect to $B = 0$ ³³⁻³⁵. **b**, Clear quasi-double-periodic $I_c(B)$ oscillations in Device A shows no hysteresis within $\sim \pm 0.3$ mT. **c**, Wider range sweep (± 2.5 mT) shows neither hysteresis nor mirror-symmetric behaviors. All data are measured at 100 mK.



Supplementary Fig. 16. Ruling out ferromagnetism with coercive field up to ± 12 T in $\text{Al-K}_2\text{Cr}_3\text{As}_3$ SQUIDs: **a, b**, $I_c(B)$ oscillations of Device C measured by stepping down (up) B , after being polarized with +12 T (-12 T) field. **c, d**, similar measurement of $I_c(B)$ oscillations in Device E. $T = 10$ mK.

We also note that neutron scattering measurements³⁸ identify the short-range spin polarization which flips on the atomic scale. Such spin structure with sub-nanometer scale will be averaged out in the micron-scale devices and cannot be the cause for our observed π -phase shift. A very weak internal field $\sim 0.3 \mu\text{T}$ has also been found in $\text{K}_2\text{Cr}_3\text{As}_3$ by muon scattering measurement³⁹, which should also be short-ranged and the overall effect should be averaged out in our devices. Moreover, the SQUID oscillation has a periodic $\sim 50 \mu\text{T}$, more than two orders larger than the internal field of $0.3 \mu\text{T}$. In Figs. 3a and 3f of the main text, the weight of the $0-\pi$ components is adjusted by a magnetic field of $\sim 2 \text{ mT}$, more than three-orders larger than the internal field. Any π -phase shift caused by $0.3 \mu\text{T}$ field is clearly not consistent with our observation where the magnetic modulation of the π phase shift happens in the scale of $\sim 50 \mu\text{T} - 2 \text{ mT}$. Finally, even if we assume the very weak internal field $\sim 0.3 \mu\text{T}$ as the coercive field of the possible ferromagnetic order, such scenario would result in a qualitatively different interference pattern⁴⁰. As illustrated in Supplementary Fig. 17a, so long as B passes $0.3 \mu\text{T}$, the spin polarization will be flipped and the $I_c(B)$ will switch to the branch of the opposite polarization. This will produce an overall mirror-symmetric $I_c(B)$, which is qualitatively different from our data in Supplementary Fig. 17b.

Expected $I_c(B)$ with weak ferromagnetism of $B_c = 0.3 \mu\text{T}$



Supplementary Fig. 17. Disagreement between our data and a weak internal magnetism of $0.3 \mu\text{T}$: **a**, Illustration of the expected $I_c(B)$ in the SQUID with a small coercive field of $0.3 \mu\text{T}$. The up (red) and down sweeps (black) should also display symmetric pattern with $B = 0$ ⁴⁰. The section beyond the coercive field is marked as dashed lines. **b**, Zoomed-in data $I_c(B)$ reproduced from Supplementary Fig. 12b showing no symmetric pattern with $B = 0$, inconsistent with the weak ferromagnetism.

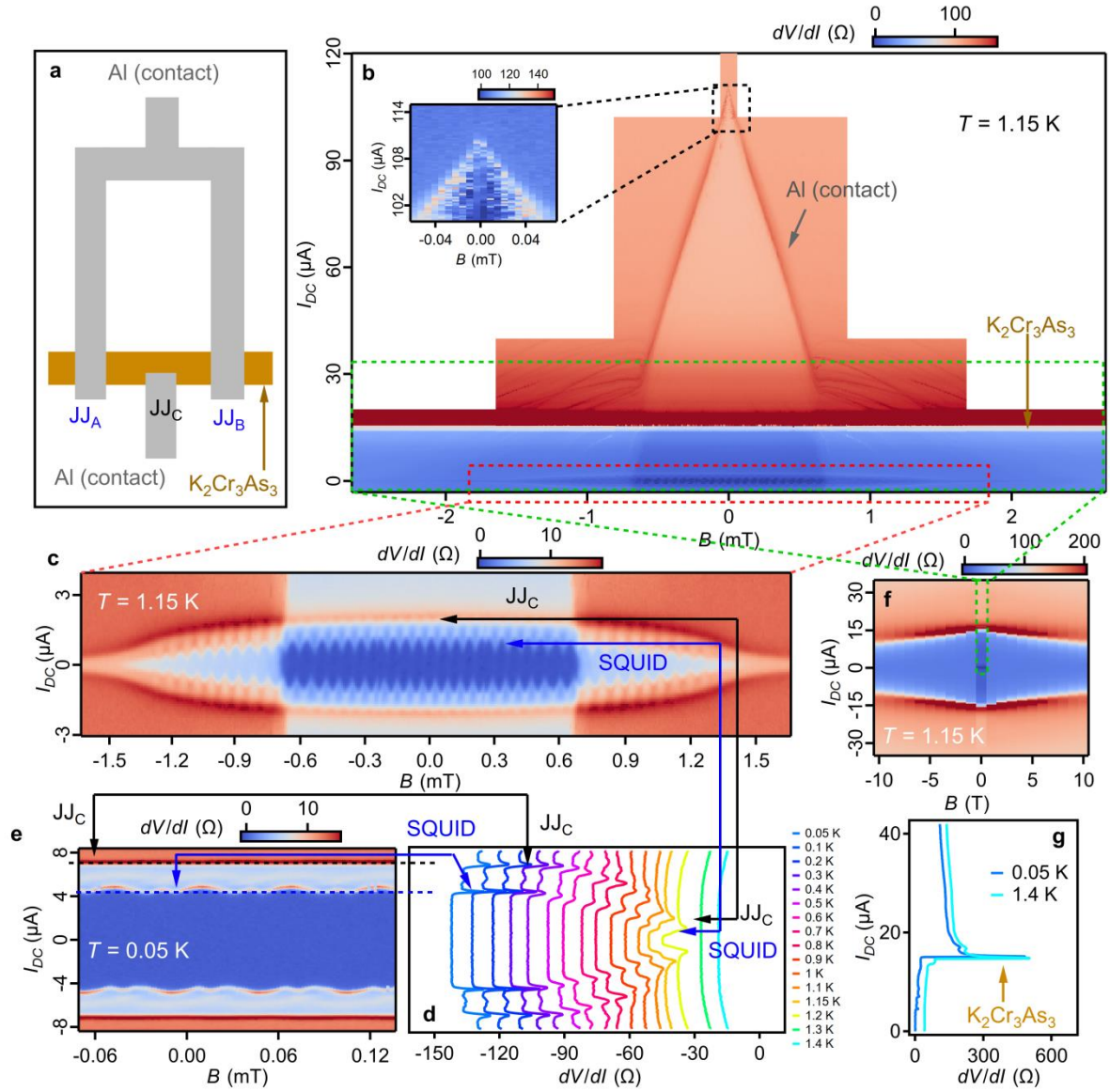
With the above evidences, we can confidently rule out the ferromagnetic impurities, the short-range magnetism, or the weak internal field in $\text{K}_2\text{Cr}_3\text{As}_3$ as the origins for our observed π -phase shift.

12 Contribution of various segments to the SQUID transport

The SQUID used in the main text involves two kinds of superconductors, namely the $\text{K}_2\text{Cr}_3\text{As}_3$ stripes and the s -wave superconductor Al. As drawn in Fig. 1 and reproduced here in Supplementary Fig. 18a, there are three JJs: $\text{JJ}_{\text{A,B}}$ and the Al ring forming the SQUID, and JJ_{C} in series with the SQUID. Both the SQUID ring and JJ_{C} are further connected by Al to the external measurement circuit (contacts). In this section, we carefully characterize the transport features associated with each component. The measurement is first done at $T = 1.15$ K in order to reduce the critical current of the device. Supplementary Figure 18b is the $dV/dI(I_{\text{DC}}, B)$ in a wide range. A horizontal blue band with the boundary marked by the brown arrow corresponds to the critical current of $\text{K}_2\text{Cr}_3\text{As}_3$. Indeed, $I_c \approx 15$ μA persists up to 10 T (Supplementary Fig. 18f) and does not change up to $T = 1.4$ K (Supplementary Fig. 18g), in agreement with the previous work on the bulk crystal^{3,4}.

By zooming in the area at low bias (Supplementary Fig. 18c), the regular oscillation is seen in the lower I_c (blue arrow), which must come from the SQUID. The upper I_c (black arrow) occurs at a finite-resistance state, indicating its origin as a component in series with the SQUID. The evolutions of the two I_c in $dV/dI(I_{\text{DC}})$ with T (Supplementary Fig. 18d) trace closely the diminishing gap of Al up to $T = 1.2$ K, which means they arise from the junctions $\text{JJ}_{\text{A,B,C}}$ with one superconducting electrode as Al. At a lower temperature $T = 0.05$ K (Supplementary Fig. 18e), the two I_c are well separated. The lower I_c clearly oscillates with flux while the upper I_c does not oscillate at all, which unequivocally confirms the earlier statement that the lower I_c belongs to the entire SQUID and the higher I_c belongs to JJ_{C} in series to the SQUID. Another feature marked by the gray arrow in Supplementary Fig. 18b has much higher I_c up to 110 μA at zero field, see the inset) and a small B_c (around 0.7 mT at zero bias). It also changes sensitively with $T < 1$ K, in agreement with the behavior of the bulk Al. We use the maxima of this I_c to calibrate zero field because it is very sensitive to B . Meanwhile, from Supplementary Fig. 18c, such contribution is in series with the SQUID and JJ_{C} , which indicates that such contribution comes from the larger

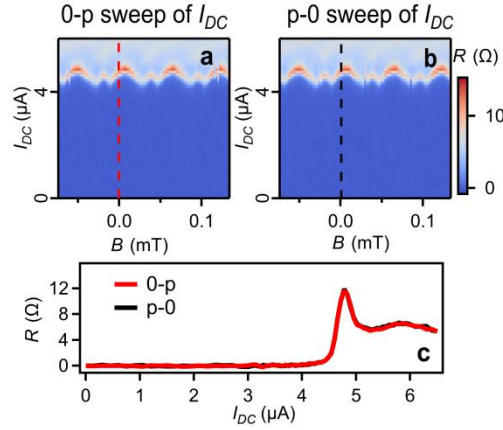
and further Al contacts connecting them. The fact that Al in the SQUID and the contacts have two separate B_c and I_c is possibly due to their different geometry. The different field profile near the $K_2Cr_3As_3$ stripes may also make the superconductivity of Al near JJ_C more robust than that of the further away contacts. In summary, the several features arising from JJ_C and the Al contacts are in series with the SQUID, and thus do not affect the analysis of the I_c oscillating with flux which is entirely determined by $JJ_{A,B}$ inside the SQUID.



Supplementary Fig. 18. Contribution of various components to the SQUID transport. **a**, Schematic of Device A. **b**, Wide range $dV/dI(I_{DC}, B)$ at $T = 1.15$ K showing bulk $K_2Cr_3As_3$ (brown arrow) and Al critical currents (gray arrow). **c**, Zoomed-in $dV/dI(I_{DC}, B)$ (red dashed rectangle) showing SQUID oscillation (blue arrow) and JJ_C contribution in series (black arrow). **d**, $dV/dI(I_{DC})$ at $B = 0$ and various T . The SQUID and JJ_C contributions are in series and well separated at low T . **e**, $dV/dI(I_{DC}, B)$ at $T = 0.05$ K with clearly separated I_c . The one from JJ_C shows no SQUID oscillations. **f**, High field $dV/dI(I_{DC}, B)$ showing $K_2Cr_3As_3$ supercurrent up to 10 T. The green dashed rectangle contains **b** data. **g**, Wide range $dV/dI(I_{DC})$ at $B = 0$ showing I_c of $K_2Cr_3As_3$ insensitive to T up to 1.4 K.

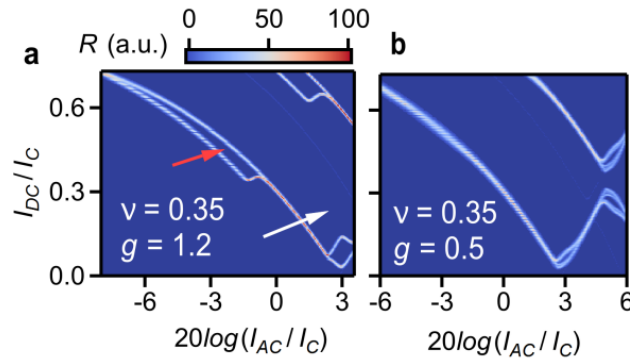
13 Half-integer Shapiro steps in ϕ -junction

Supplementary Figure 19 shows the measurements of Device A where the I_{DC} is swept from superconducting to normal states (0-p, Supplementary Fig. 19a) and from normal to superconducting states (p-0, Supplementary Fig. 19b). The transition current is the switch current I_c and retrap current I_r respectively. Supplementary Fig. 19c shows a typical linecut, demonstrating $I_c = I_r$ and thus the overdamped scenario³¹ in our SQUIDs. This greatly simplifies the analysis of the phase dynamics under microwave irradiation, and it is justified to use the RSJ model³¹.



Supplementary Fig. 19. Overdamped JJs demonstrated by equal switch and retrap current.

a, b, $dV/dI(I_{DC}, B)$ for 0-p and p-0 sweeps, measuring the switch and retrap critical currents, respectively. **c**, A typical $dV/dI(I_{DC})$ taken from the same B in **a, b**. No hysteresis is observed.



Supplementary Fig. 20. ϕ -JJ state revealed by the half-integer steps. a, b, Calculated

$dV/dI(I_{DC}/I_C, 20\log(I_{AC}/I_C))$ by Supplementary Equation (S3). $\nu = f/f_J = 0.35$ same as the main text Fig. 4 and 2h. $g = |I_2/I_1| = 1.2$ (a) and 0.5 (b), respectively. The half-integer steps (red arrows) between the integer steps (white arrows) before the first node are only visible for $g > 1/2$.

Considering the SQUID as a whole system with the flux-tunable CPR $I_{\text{tot}}(\varphi, \Phi)$, where the flux Φ through the SQUID is fixed when calculating the Shapiro steps. Therefore, for the phase drop φ across the whole SQUID, we have⁴¹:

$$\frac{d\varphi}{d\tau} + i_{\text{tot}}(\varphi, \Phi) = i_{DC} + i_{AC} \cos(2\pi\nu\tau) \quad (\text{S3})$$

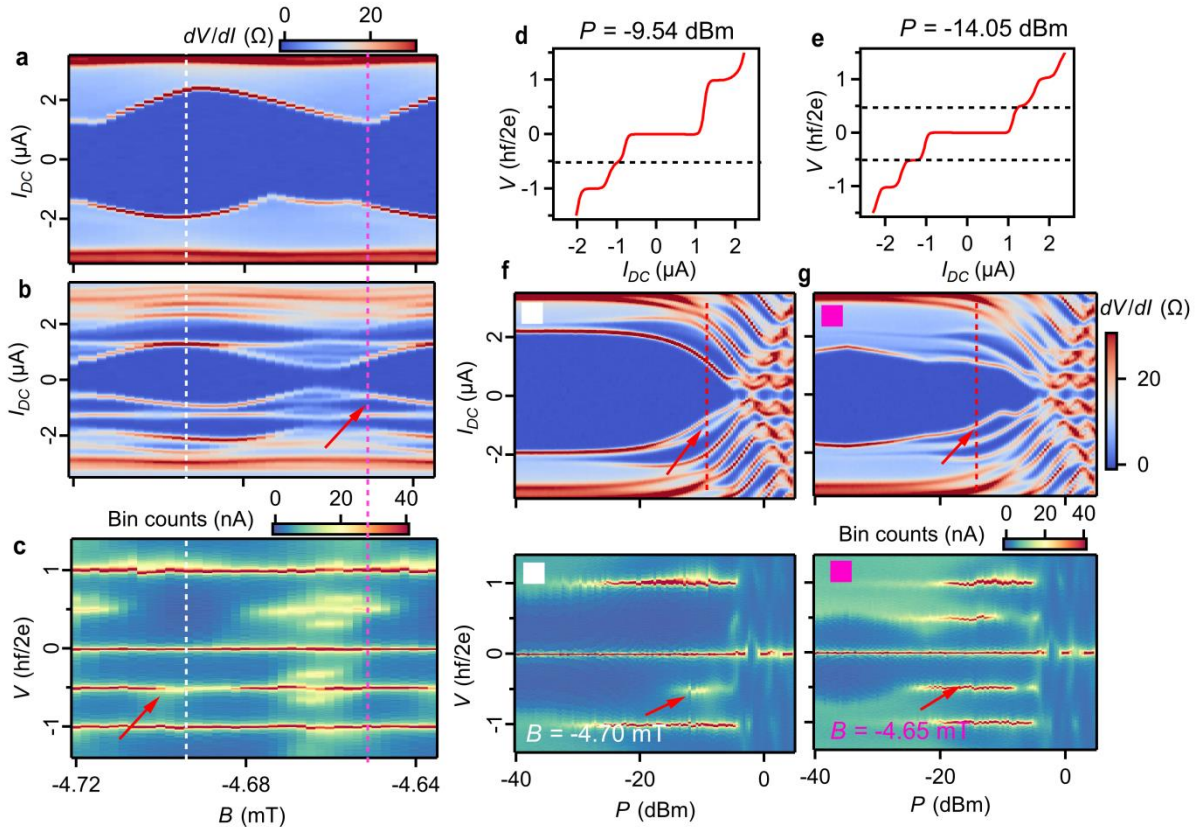
where $i_{\text{tot}} = I_{\text{tot}}/I_C$, $i_{DC} = I_{DC}/I_C$, and $i_{AC} = I_{AC}/I_C$ are SQUID supercurrent, the d.c. bias current, and the a.c. current induced by the microwave respectively, all normalized by the critical current of the SQUID. The Josephson frequency of the system is $f_J = 2eI_C R/\hbar$ where R is the normal resistance. In Supplementary Equation (S3), $\nu = f/f_J$ and $\tau = f_J t$ are the normalized irradiation frequency and time.

Modeling $i_{\text{tot}}(\varphi) = I_1/I_C \sin(\varphi) - I_2/I_C \sin(2\varphi)$, the Shapiro map of the averaged differential resistance $dV/dI(i_{AC}, i_{DC})$ is determined by $g = |I_1/I_2|$ and ν . In the main text Fig. 4a (reproduced in Supplementary Figs. 20a), we show that for $g = 1.2 > 1/2$, the Shapiro map exhibits the 1/2 Shapiro step (red arrows) between sequential integer Shapiro steps. Importantly, in Supplementary Fig. 20b with the same ν but with $g = 1/2$, only integer steps (white arrow) are seen.

Supplementary Figure 21 shows the microwave response for $\nu = f/f_J = 0.35$ of Device B shown in Supplementary Fig. 11. Interestingly, in the field range where I_{C-} shows the quasi-double-periodic oscillations, I_{C+} only shows the single-periodic oscillations. There, we reproduce the clear and continuous 1/2 step (Supplementary Figs. 21b, c (red arrows)) also only for the negative I_{DC} . The Shapiro maps (Supplementary Figs. 21f, g) are taken at B indicated by the vertical dashed lines in Supplementary Figs. 21a-c. In all of the Shapiro maps, a clear 1/2 step (red arrows, highlighted by the V-I curves in Supplementary Figs. 21d, e) similar to Supplementary Fig. 20a shows up only for the negative I_{DC} with quasi-double-periodic feature and disappears for the positive I_{DC} with single-periodic feature. These observations further confirm that a robust and dominant second

harmonics is the source for both the quasi-double-periodic feature and the 1/2 Shapiro step for the negative I_{DC} .

We note that although the half-integer steps may appear in quasi-ballistic JJs for larger frequencies and power⁴¹, for the low frequency (much lower than f_J) and power (for example, before the first node) used in our experiment, the emergence of 1/2 step can be used as an indicator for the $g > 1/2$ in our system^{28,42-44}. In the main text, we also exclude other alternative mechanisms such as interference effect⁴⁵ and non-equilibrium. In particular, the comparison between positive and negative bias in Device B clearly shows that This further eliminates the interpretation of the quasi-double-periodic $I_c(B)$ as the beating between two single-periodic oscillating channels¹⁵, since the beating effect does not induce large second harmonics. Therefore, the measured quasi-double periodic $I_c(B)$, as well as the robust half-integer Shapiro steps, can only be caused by the co-existence of 0- and π -phases supercurrent.



Supplementary Fig. 21. Device B reproducing continuous 1/2 Shapiro step: a, $dV/dI(I_{DC}, B)$

without microwave at $T = 96$ mK, showing quasi-double-periodic oscillations for negative bias and single-periodic oscillations for positive bias. **b**, **c**, $dV/dI(I_{DC}, B)$ and the converted histograms with the irradiation of $f = 3.38$ GHz (or $\nu = 0.35$, $I_c = 2.0$ μ A, $R_N = 9.9$ Ω) and $P = -10$ dBm. The 1/2 step (red arrow) is continuous over the whole period only for the negative bias. **d**, V - I curve at $P = -9.56$ dBm and $B = -4.696$ mT (integration of the red dashed line R - I in **f**), showing 1/2 step (dashed line). **e**, Similar V - I curve at $P = -14.05$ dBm and $B = -4.646$ mT marked by the red dashed line in **g**. **f**, $dV/dI(I_{DC}, P)$ (upper) and the converted histogram (lower) at $B = -4.696$ mT (the white vertical dashed lines in **a-c**), confirming the robust 1/2 step (red arrows). **g**, Similar to **f** but with $B = -4.646$ mT (the magenta vertical dashed lines in **a-c**), all showing clear 1/2 step.

References

1. Mu, Q.-G., Ruan, B.-B., Pan, B.-J., Liu, T., Yu, J., Zhao, K., Chen, G.-F., Ren, Z.-A.: Ion-exchange synthesis and superconductivity at 8.6 K of $\text{Na}_2\text{Cr}_3\text{As}_3$ with quasi-one-dimensional crystal structure. *Phys. Rev. Mater.* **2**, 034803 (2018).
2. Chen, R.Y., Wang, N.L.: Progress in Cr- and Mn-based superconductors: a key issues review. *Reports on Progress in Physics* **82**(1), 012503 (2018).
3. Bao, J.-K., Liu, J.-Y., Ma, C.-W., Meng, Z.-H., Tang, Z.-T., Sun, Y.-L., Zhai, H.-F., Jiang, H., Bai, H., Feng, C.-M., Xu, Z.-A., Cao, G.-H.: Superconductivity in quasi-one-dimensional $\text{K}_2\text{Cr}_3\text{As}_3$ with significant electron correlations. *Phys. Rev. X* **5**, 011013 (2015).
4. Pang, G.M., Smidman, M., Jiang, W.B., Bao, J.K., Weng, Z.F., Wang, Y.F., Jiao, L., Zhang, J.L., Cao, G.H., Yuan, H.Q.: Evidence for nodal superconductivity in quasi-one-dimensional $\text{K}_2\text{Cr}_3\text{As}_3$. *Phys. Rev. B* **91**, 220502 (2015).
5. Wu, X., Yang, F., Le, C., Fan, H., Hu, J.: Triplet p_z -wave pairing in quasi-one-dimensional $\text{A}_2\text{Cr}_3\text{As}_3$ superconductors ($A = \text{K}, \text{Rb}, \text{Cs}$). *Phys. Rev. B* **92**, 104511 (2015).
6. Jiang, H., Cao, G., Cao, C.: Electronic structure of quasi-one-dimensional superconductor

- $\text{K}_2\text{Cr}_3\text{As}_3$ from first-principles calculations. *Scientific Reports* **5**(1), 16054 (2015).
7. Geshkenbein, V.B., Larkin, A.I., Barone, A.: Vortices with half magnetic flux quanta in “heavy-fermion” superconductors. *Phys. Rev. B* **36**, 235–238 (1987).
 8. Tsuei, C.C., Kirtley, J.R.: Pairing symmetry in cuprate superconductors. *Rev. Mod. Phys.* **72**, 969–1016 (2000).
 9. Van Harlingen, D.J.: Phase-sensitive tests of the symmetry of the pairing state in the high-temperature superconductors—evidence for $d_{x^2-y^2}$ symmetry. *Rev. Mod. Phys.* **67**, 515–535 (1995).
 10. Lindström, T., Johansson, J., Bauch, T., Stepantsov, E., Lombardi, F., Charlebois, S.A.: Josephson dynamics of bicrystal d -wave $\text{YBa}_2\text{Cu}_3\text{O}_{7-\delta}$ dc-SQUIDs. *Phys. Rev. B* **74**, 014503 (2006).
 11. Bauch, T., Johansson, J., Cedergren, K., Lindström, T., Lombardi, F.: YBCO SQUIDs with unconventional current phase relation Author links open overlay panel. *Physica C* **463** – 465 (2007).
 12. Desbiolles, B.X.E., Bertsch, A. & Renaud, P. Ion beam etching redeposition for 3D multimaterial nanostructure manufacturing. *Microsyst Nanoeng* **5**, 11 (2019).
 13. Wang, Y. & Fu, L. Topological phase transitions in multicomponent superconductors. *Phys. Rev. Lett.* **119**, 187003 (2017).
 14. Barash, Y. S., Burkhardt, H. & Rainer, D. Low-temperature anomaly in the Josephson critical current of junctions in d -wave superconductors. *Phys. Rev. Lett.* **77**, 4070–4073 (1996).
 15. Murani, A., Kasumov, A., Sengupta, S., Kasumov, Yu A., Volkov, V. T. Khodos, I. I. Brisset, F. Delagrangé, R., Chepelianskii, A., Deblock, R., Bouchiat, H., Guéron, S.: Ballistic edge states in Bismuth nanowires revealed by SQUID interferometry. *Nature Communications* **8**, 15941 (2017).
 16. Bernard, A., Peng, Y., Kasumov, A., Deblock, R., Ferrier, M., Fortuna, F., Volkov, V. T., Kasumov, Yu. A., Oreg, Y., von Oppen, F., Bouchiat H., Guéron, S.: Long-lived Andreev

- states as evidence for protected hinge modes in a bismuth nanoring Josephson junction. *Nature Physics* **19**, 358–364 (2023).
17. Proakis, J.G.: *Digital Signal Processing: Principles Algorithms and Applications*. Prentice Hall, New Jersey (2001).
 18. Meservey, R., Tedrow, P.M.: Measurements of the kinetic inductance of superconducting linear structures. *Journal of Applied Physics* **40**(5), 2028–2034 (2003).
 19. Annunziata, A.J., Santavicca, D.F., Frunzio, L., Catelani, G., Rooks, M.J., Frydman, A., Prober, D.E.: Tunable superconducting nanoinductors. *Nanotechnology* **21**(44), 445202 (2010).
 20. Sickinger, H., Lipman, A., Weides, M., Mints, R.G., Kohlstedt, H., Koelle, D., Kleiner, R., Goldobin, E.: Experimental evidence of a φ Josephson junction. *Phys. Rev. Lett.* **109**, 107002 (2012).
 21. Goldobin, E., Koelle, D., Kleiner, R., Mints, R.G.: Josephson junction with a magnetic-field tunable ground state. *Phys. Rev. Lett.* **107**, 227001 (2011).
 22. Goldobin, E., Kleiner, R., Koelle, D., Mints, R.G.: Phase retrapping in a pointlike φ Josephson junction: The butterfly effect. *Phys. Rev. Lett.* **111**, 057004 (2013).
 23. Goldobin, E., Koelle, D., Kleiner, R., Buzdin, A.: Josephson junctions with second harmonic in the current-phase relation: Properties of φ junctions. *Phys. Rev. B* **76**, 224523 (2007).
 24. Mannhart, J., Hilgenkamp, H., Mayer, B., Gerber, C., Kirtley, J.R., Moler, K.A., Sigrist, M.: Generation of magnetic flux by single grain boundaries of $\text{YBa}_2\text{Cu}_3\text{O}_{7-x}$. *Phys. Rev. Lett.* **77**, 2782–2785 (1996).
 25. Mints, R.G.: Self-generated flux in Josephson junctions with alternating critical current density. *Phys. Rev. B* **57**, 3221–3224 (1998).
 26. Tsuei, C.C., Kirtley, J.R., Chi, C.C., Yu-Jahnes, L.S., Gupta, A., Shaw, T., Sun, J.Z., Ketchen, M.B.: Pairing symmetry and flux quantization in a tricrystal superconducting ring of $\text{YBa}_2\text{Cu}_3\text{O}_{7-\delta}$. *Phys. Rev. Lett.* **73**, 593–596 (1994).

27. Lindström, T., Charlebois, S.A., Tzalenchuk, A.Y., Ivanov, Z., Amin, M.H.S., Zagorskin, A.M.: Dynamical effects of an unconventional current-phase relation in YBCO dc SQUIDS. *Phys. Rev. Lett.* **90**, 117002 (2003).
28. Stoutimore, M.J.A., Rossolenko, A.N., Bolginov, V.V., Oboznov, V.A., Rusanov, A.Y., Baranov, D.S., Pugach, N., Frolov, S.M., Ryazanov, V.V., Van Harlingen, D.J.: Second-harmonic current-phase relation in Josephson junctions with ferromagnetic barriers. *Phys. Rev. Lett.* **121**, 177702 (2018).
29. Yip, S., Josephson current-phase relationships with unconventional superconductors *Phys. Rev. B* **52**, 3087 (1995).
30. Yang, J., Luo, J., Yi, C., Shi, Y., Zhou, Y., Zheng, G.-Q.: Spin-triplet superconductivity in $K_2Cr_3As_3$. *Science Advances* **7**(52), 4432 (2021).
31. Tinkham, M.: Introduction to Superconductivity. International series in pure and applied physics. McGraw Hill, New York (1996).
32. Ai, L., Zhang, E., Yang, J., Xie, X., Yang, Y., Jia, Z., Zhang, Y., Liu, S., Li, Z., Leng, P., Cao, X., Sun, X., Zhang, T., Kou, X., Han, Z., Xiu F., Dong, S.: Van der Waals ferromagnetic Josephson junctions. *Nat Commun* **12**, 6580 (2021).
33. Kapran, O. M., Iovan, A., Golod, T., Krasnov, V. M.: Observation of the dominant spin-triplet supercurrent in Josephson spin valves with strong Ni ferromagnets. *Phys. Rev. Research* **2**, 013167 (2020).
34. Petković, I., Aprili, M., Barnes, S. E., Beuneu, F., Maekawa, S.: Direct dynamical coupling of spin modes and singlet Josephson supercurrent in ferromagnetic Josephson junctions *Phys. Rev. B* **80**, 220502(R) (2009).
35. X. Ye, J. Cook, E. D. Huemiller, A. D. K. Finck, P. Ghaemi, T. Vojta, V. P. Adiga, S. R. Saha, J. Paglione, and C. Kurter: Unconventional Josephson junctions with topological Kondo insulator weak links *Phys. Rev. B* **100**, 104505 (2019)
36. Suominen, H. J., Danon, J., Kjaergaard, M., Flensberg, K., Shabani, J., Palmstrøm, C. J.,

- Nichele, F., Marcus, C. M.: Anomalous Fraunhofer interference in epitaxial superconductor-semiconductor Josephson junctions. *Phys. Rev. B* **95**, 035307 (2017).
37. T. Golod, V. M. Krasnov: Demonstration of a superconducting diode-with-memory, operational at zero magnetic field with switchable nonreciprocity. *Nat. Commun.* **13**, 3658 (2022).
 38. K.M. Taddei, Q. Zheng, A.S. Sefat, C. de la Cruz: Coupling of structure to magnetic and superconducting orders in quasi-one-dimensional $\text{K}_2\text{Cr}_3\text{As}_3$. *Phys. Rev. B* **96**, 180506(R) (2017).
 39. Adroja, D. T., Bhattacharyya, A., Telling, M., Feng, Y., Smidman, M., Pan, B., Zhao, J., Hillier, A. D., Pratt, F. L., Strydom, A. M.: Superconducting ground state of quasi-one-dimensional $\text{K}_2\text{Cr}_3\text{As}_3$ investigated using μSR measurements. *Phys. Rev. B* **92**, 134505 (2015).
 40. Glick, J. A., Loloee, R., Pratt, W. P. & Birge, N. O. Critical current oscillations of Josephson junctions containing PdFe manomagnets. *IEEE Trans. Appl. Supercond.* **27**, 1800205 (2017).
 41. Raes, B., Tubsrinuan, N., Sreedhar, R., Guala, D.S., Panghotra, R., Dausy, H., Souza Silva, C.C., Vondel, J.: Fractional Shapiro steps in resistively shunted Josephson junctions as a fingerprint of a skewed current-phase relationship. *Phys. Rev. B* **102**, 054507 (2020).
 42. Zhao, S.Y.F., Cui, X., Volkov, P.A., Yoo, H., Lee, S., Gardener, J.A., Akey, A.J., Engelke, R., Ronen, Y., Zhong, R., Gu, G., Plugge, S., Tummuru, T., Kim, M., Franz, M., Pixley, J.H., Poccia, N., Kim, P.: Time-reversal symmetry breaking superconductivity between twisted cuprate superconductors. *Science* **382**, 6677, 1422-1427 (2023).
 43. Sellier, H., Baraduc, C., Lefloch, F.m.c., Calemczuk, R.: Half-integer shapiro steps at the $0-\pi$ crossover of a ferromagnetic josephson junction. *Phys. Rev. Lett.* **92**, 257005 (2004)
 44. Terpstra, D., IJsselsteijn, R.P.J., Rogalla, H.: Subharmonic Shapiro steps in high- T_c Josephson junctions. *Applied Physics Letters* **66**(17), 2286–2288 (1995).
 45. Souto, R.S., Leijnse, M., Schrade, C.: Josephson diode effect in supercurrent interferometers.

Phys. Rev. Lett. **129**, 267702 (2022).

46. Iorio, A., Crippa, A., Turini, B., Salimian, S., Carrega, M., Chirolli, L., Zannier, V., Sorba, L., Strambini, E., Giazotto, F., Heun, S.: Half-integer Shapiro steps in highly transmissive InSb nanoflag Josephson junctions. Phys. Rev. Res. 5, 033015 (2023).